Investigation of a Microgravimetric Sensor and an Application to the Detection of Protein-Antibody Interaction

by

M. Salih Kılıç

A Thesis Submitted to the
Graduate School of Engineering
in Partial Fulfillment of the Requirements for
the Degree of

Master of Science
in
Mechanical Engineering

Koc University
September 2009

Koc University

Graduate School of Sciences and Engineering

This is to certify that I have examined this copy of a master's thesis by

M. Salih Kılıç

and have found that it is complete and satisfactory in all respects,
and that any and all revisions required by the final
examining committee have been made.

Committee Members:

B. Erdem Alaca, Ph. D. (Advisor)

Hakan Ürey, Ph. D.

İ Halil Kavaklı, Ph. D.

Date: 24 September 2009

ABSTRACT

A theoretical model for a previously developed micro-mechanical resonator mass-detector (with integrated diffraction-gratings) based on high-sensitivity displacement measurements by diffraction-grating interferometry, is developed for utilization in bio-chemical mass sensing applicatons. The model is verified by theoretical examples and an experimental testing procedure. The detection of a specific protein-antibody, human k-opioid (hKOR) receptor protein and hKOR-antibody, interaction is demonstrated as an example of a selective bio-sensing application.

ÖZET

Daha önce geliştirilen kırınım-ızgarasi-enterferometresi tabanlı yüksek-hassasiyetli deplasman ölçümüne dayalı, (tümleşik kırınım ızgaralı) kütle-ölçer mikro-mekanik çınlaçların bio-kimyasal kütle ölçüm uygulamalarında kullanımı için kuramsal bir modelleme geliştirildi. Bu modelin, kuramsal örnekler ve inorganik bir deneyle doğrulaması yapıldı. Organik deneysel bir uygulama olmak üzere belirli bir biyolojik etkileşim (olan hKOP-antikor etkileşimi) tespiti biyo-seçici olarak gerçekleştirildi.

ACKNOWLEDGEMENTS

I would like to express my utmost gratitude to my thesis advisor Dr. B. Erdem Alaca for his continuous support, excitement and encouragement throughout my research, which made me feel the same excitement and have fun during this period.

I would also like to sincerely thank to Dr. Hakan Urey and Dr. I. Halil Kavakli for kindly taking part in my thesis comitee and for their precious contributions.

I gratefully acknowledge TUBITAK BIDEB for providing the scholarship for my graduate study. I thank TUBITAK and Koc University for improving the research environment and increasing the quality and importance of academic study with their invaluable support.

I would also like to thank my colleagues for their valuable help and support during my research. I want to thank Serhat Yavuz for his help and company during those long periods of fabrication, measurement, literally for many days and nights. I want to thank Natali Ozber, for her biological expertise on functionalisation procedures. I also want to thank Selim Olcer, Onur Ferhanoglu, Erdem Erden and all other OML (Optical Microsystems Laboratory) members for their patience and essential help while using various equipments for measurements.

Finally, I want to thank all my family for their endless love and support.

This study is supported by TUBITAK under grant No 105 E148.

TABLE OF CONTENTS

List of Tables ix

List of Figures x

Nomenclature xii

Chapter 1: Introduction 1-4

Chapter 2: Theoretical Model 5-19

2.1 Overview 5

2.2 Resonant Mass Detection Method in the Literature. 6

2.3 Additional Effect of Stiffness Change on Resonance Frequency. 8

2.4 Theoretical Verification 11

2.4.1 Sample Cases. 11

2.4.2 Results. 12

2.5 Experimental Verification. 15

2.5.1 Experimental Setup & Procedure. 15

2.5.2 Results. 17

2.6 Conclusion. 18

Chapter 3: Device Fabrication 20-28

3.1 Fabrication Flow 20

3.1.1 Substrate Preparation 20

3.1.2 Seed Layer Formation . . . 21
3.1.3 Mold-Pattern Preparation: UV Photolithography . . . 22
3.1.4 Micro-cantilever Structure Formation . . . 22
3.1.5 Releasing the Micro-cantilevers: Wet Etch . . . 23
3.1.6 Final Cleaning . . . 25
3.2 Encountered Problems . . . 25
3.2.1 Delamination Due to Crocodile Tips . . . 25
3.2.2 Excessive Undercuts Due to Over-etched Cr & Au Layers . . . 27
3.2.3 Stiction Due to High Si Etch Rate . . . 28
3.3 Conclusion . . . 28

Chapter 4: Measurement Setup & Procedure 29-41

4.1 Actuation Setup . . . 29
4.2 Photo-detector Setup . . . 30
4.3 Noise Immunity of the Setup . . . 33
4.4 Improvements on the Setup . . . 35
4.4.1 Removal of the Current Amplifier . . . 35
4.4.2 Signal Amplitude . . . 35
4.4.3 Laser Spot Size . . . 36
4.4.4 Determination of the Resonance Frequency . . . 36
4.4.5 Higher-Order Mode Resonance Frequencies . . . 37
4.5 Measurement Procedure . . . 39
4.5 Conclusion . . . 41

Chapter 5: Results & Discussion **42-53**

5.1 Fabrication Process Variations. 42

5.2 Selective Detection of Protein-Antibody Interaction 47

Chapter 6: Conclusion & Outlook **54-56**

6.1 Conclusion. 54

6.2 Outlook. 55

Appendix A: Modal Analysis of a Uniform Bilayer Bernoulli Beam With an End Load **57-42**

A.1 Uniform Bilayer Rectangular Bernoulli Beam. 57

A.2 Uniform Bilayer Rectangular Bernoulli Beam with an End Load. . . . 61

Bibliography **62-64**

Vita **65**

LIST OF TABLES

Table 2.1: Reponsivity Results 18

Table 2.2: Calibration Results 18

Table 4.1: Summarized Treatment and Measurement Protocol 39

Table 5.1 Fabrication Process Variations for Experimental Verification of the Theoretical Model 43

Table 5.2 Fabrication Process Variations for the Reference Die (Selective Detection of Protein-Antibody Interaction) 44

Table 5.3 Fabrication Process Variations for the Protein Die (Selective Detection of Protein-Antibody Interaction) 45

Table 5.4 Fabrication Process Variations for the Control Die (Selective Detection of Protein-Antibody Interaction) 46

Table 5.5 Average Shifts and Standard Deviations in Resonance Frequencies for Protein and Control Dice 49

Table 5.6: Expected and Observed Surface Mass Densities for Protein and Control Dice 52

LIST OF FIGURES

Figure 2.1: Depiction of the parameters used for the micro-cantilever modeling 10

Figure 2.2: Dependence of the frequency shift on adsorbate mass density in the case of a constant ratio of elastic moduli. 13

Figure 2.3: Dependence of the frequency shift on adsorbate elastic modulus in the case of same mass density of adsorbate and substrate. 14

Figure 2.4: Schematic depiction of a monolayer uniform Ni microcantilever 15

Figure 2.5: Schematic depiction of accumulation of a Au layer on top of a monolayer uniform Ni microcantilever 16

Figure 2.6: Schematic depiction of the 1st incremental addition of Au layer on top of the initial bilayer uniform Ni-Au microcantilever 16

Figure 2.7: Schematic depiction of the 2nd incremental addition of Au layer on top of the bilayer uniform Ni-Au microcantilever 16

Figure 2.8: The terms used in the interpretation of the results of the calibration experiment 18

Figure 3.1: Fabrication Flow 21

Figure 3.2: Electro-deposition process 23

Figure 3.3: An array of micro-cantilevers that is ready for measurement. 24

Figure 3.4: An A sample die with the main structure is torn off due to delamination. 26

Figure 3.5 A sample crocodile used for electrical contact during electro-deposition (a) before and (b) after covering with Al-folio. 27

Figure 4.1: Schematic description of the measurement setup. 29

Figure 4.2: Measurement Setup 30

Figure 4.3: Optical readout with electromagnetic actuation. 31

Figure 4.4: A sample response curve and the nonlinear fit 32

Figure 4.5 Noise Immunity Setup 33

Figure 4.6 Comparison of LDV and PD measurements for a specific cantilever 34

Figure 4.7 A sample measurement with fitted parameters (and percentage errors) 37

Figure 4.8 The first three resonance modes of a sample cantilever, both in air and in water. 38

Figure 4.9 The expected conditions of the cantilevers on the (a) Reference, (b) BSA, (c) hKOR chips after 1st and 2nd processes. 40

Figure 5.1: The average shifts in resonance frequencies of the cantilevers in three dice subjected to the procedure explained and the resulting cantilever depiction after the biochemical treatment corresponding to each die. 50-51

NOMENCLATURE

E	elastic modulus
E_0	elastic modulus of the cantilever
E_1	elastic modulus of the accreted material
E_r	ratio of elastic modulus of the accreted material to that of the cantilever
h_0	thickness of the cantilever
h_1	thickness of the accreted material
h_r	ratio of thickness of the accreted material to that of the cantilever
t	thickness of the cantilever
l	length of the cantilever
L	length of the cantilever
L_p	length of the diffraction grating platform
w	width of the cantilever
w_p	width of the diffraction grating platform
A	surface area of the cantilever (wL)
A_p	surface area of the diffraction grating platform
f_0	resonance frequency
$f_0^{'}$	new resonance frequency after accretion
k	stiffness
m	mass
m_0	mass of the cantilever
m_1	mass of the accreted material
m^*	effective mass
n	coefficient to determine the effective mass
ρ	density

ρ_0	density of the cantilever
ρ_1	density of the accreted material
ρ_r	ratio of density of the accreted material to that of the cantilever
$\mathfrak{R}$	responsivity
Q	quality factor

Chapter 1

INTRODUCTION

1.1 Overview

Micro-cantilevers can be utilized as bio-chemical sensors in order to meet the demand for cheap, fast and highly sensitive methods providing with high-throughput screening for label-free bio-chemical sensing applications. The batch silicon micromachining techniques developed (and have been utilized for decades) for integrated circuit (IC) process technology makes it possible for these miniaturized and highly sensitive sensors to be inexpensively mass-produced. [1]

Bio-chemical micro-sensors, with this high sensitivity and potential parallelization, are ideal for utilization as label-free rapid-response sensors for bio-chemical, namely protein-antibody, binding interactions, which have potential powerful use for such areas mainly as clinical diagnostics, bio-chemical laboratory research in drug industry, environmental monitoring for bio-chemical security, especially in public places, and so forth.

The main motivation of this study is to obtain a high-resolution measurable physical signal corresponding to the specific protein-antibody interaction of interest, in this case the protein being the human κ-opioid-receptor (hKOR) antigens and the antibody being hKOR-antibody (anti-His).

In the previous studies by Ocakli[1] and Ozturk[2], design, fabrication and characterization of an electromagnetically actuated cantilever sensor with integrated optical readout was accomplished. Their studies have resulted in a low-noise, highly parallelizable, robust and potentially portable mass sensing system which could be utilized for specific detection of biological analytes inside a liquid medium. Nevertheless, there were some problems waiting to be solved in both fabrication and measurement.

First, there was not a solid analytical treatment investigating the validity of the formulas that were used for characterization of the cantilevers and interpretation of the results, which created a strong need to resort to finite element analysis for almost every measurement. In addition, these formulas and relations sometimes could not explain the observed results, especially for the biological part.

Apart from that, during the fabrication, for instance, one was used to encounter a delamination problem most of the time, significantly decreasing the efficiency of the fabrication process. When the delamination did not occur, one had to deal with another major problem, the stiction of the cantilevers.

As for the measurement part, though, the system was theoretically low-noise, and not in need of a vibration isolation system, it was hard to show this powerful aspect reproducibly.

All these problems used to consume so much time for both fabricating a usable device and interpreting the results obtained by this device.

This thesis, therefore, focuses on improving the fabrication, providing a solid analytical treatment for characterization of the cantilevers and making use of the powerful aspects of the utilized optical readout method, namely diffraction grating interferometry, and later using this sensor mechanism to selectively detect a specific protein-antibody interaction, namely hKOR and hKOR-antibody interaction.

1.2 Outline

This thesis in total is composed of 6 chapters and appendix:

In Chapter 2, Theory, after a brief introduction on the general approach, neglecting the effect of stiffness change, in the literature, a solid analytical treatment is carried out in order to establish a more accurate theoretical model for the dependence of the natural (resonance) frequency of a uniform bilayer cantilever with an integrated diffraction grating, on its stiffness and mass. This theoretical model is used to investigate the effects of stiffness change in addition to the mass change, on the shift in resonance frequency. The model is verified by both theoretical and experimental examples. The suggestions resulting from the investigation of these example cases are then discussed.

In Chapter 3, Device Fabrication, the fabrication flow and the solutions to the encountered problems, some of which are mentioned above, during the fabrication are briefly explained.

In Chapter 4, Measurement Setup & Procedure, the measurement setup and some improvements carried out on the setup are examined, followed by the experimental procedure for the bio-selective detection of protein-antibody interaction.

In Chapter 5, Results & Discussion, the fabrication process variations and results of the protein-antibody interaction experiment, for which the experimental procedure is given in Chapter 4, are presented and discussed.

In Chapter 6, Conclusion & Outlook, what has been carried out in the course of the study is summarized with an outlook for further improvements that can be made especially for the measurement parts.

In Appendix A, the details for the derivation of the theoretical formula for the shift in the resonance frequency is provided.

Chapter 2

THEORETICAL MODEL

2.1 Overview

In the resonant mass detection method, the resonance frequency is monitored with an appropriate readout mechanism. When an extra mass accretes on the cantilever surface, a shift in the resonance frequency of the cantilever is observed which is quantitatively related to this mass accretion. The amount of this shift is a function of various parameters including the position of where the accretion occurs [4], cantilever stiffness [5], utilized mode, etc.

In the following parts of this chapter, some general aspects of resonant mass detection method reported in literature, regarding what is being sensed by the sensors reported, will be explained briefly. Afterwards, a more solid theoretical model, mainly to isolate stiffness and mass effects for the micro-cantilevers fabricated and used during the course of this thesis, is developed. This theoretical model shows a clear diversion from the general approach in the literature, which accounts responsible the change in the resonator's mass only for the change in its resonance frequency and is incapable of explaining the positive shifts observed both during the study and the results reported by many other researchers [5, 6, 7].

2.2 Resonant Mass Detection Method in the Literature

The resonance frequency of the first mode of a cantilever, in terms of its stiffness and effective mass is defined as,

$$f_0 = \frac{1}{2\pi}\sqrt{\frac{k}{m*}} \tag{2.1}$$

where $k = \frac{Ewt^3}{4l^3}$ is the stiffness and $m* = n(\rho wlt)$ is the effective mass of the cantilever beam, constant n ($0<n<1$) depending on the geometry, ρ is the density and w, t and l are, respectively, width, thickness and length of the cantilever beam. For the case of a simple one-end-fixed rectangular cantilever beam n is equal to 0.24 [8, 9]. Consequently, the resonance frequency can alternatively be expressed as,

$$f_0 = 0.162\frac{t}{l^2}\sqrt{\frac{E}{\rho}} \tag{2.2}.$$

If an effective extra mass $\Delta m*$ accretes on a cantilever, the resonance frequency of the cantilever changes from f_0 to f_0':

$$f_0' = \frac{1}{2\pi}\sqrt{\frac{k}{m*+\Delta m*}} \tag{2.3}$$

In equation 2.8, $\Delta m^* = \Delta m$ if the mass is accumulated only on the free end of the cantilever and $\Delta m^* = 0.24\Delta m$ if the mass is uniformly distributed onto the surface of the

cantilever beam. Assuming the stiffness of the cantilever remains unchanged after mass loading, the mass, only, responsible for the shift in resonance frequency can be calculated as:

$$\Delta m^* = \frac{k}{4\pi^2}\left(\frac{1}{f_0'^2} - \frac{1}{f_0^2}\right) \tag{2.4}$$

The sensitivity of the cantilevers has been defined in different ways. Starting from the first order approximation to the Taylor expansion of the changed resonance frequency of the micro-cantilever around the initial resonance frequency as a function of its mass (assuming other material properties unchanged), the shift in the resonance frequency can be written as,

$$\Delta f_0 \approx \frac{\partial f_0}{\partial m^*}\Delta m^* = \frac{-f_0}{2m^*}\Delta m^* \tag{2.5}$$

Thus, one such definition of sensitivity is given as,

$$\Re = \frac{\partial f_0}{\partial m^*} = \frac{-f_0}{2m^*} \tag{2.6}$$

where $\Re$ is the *mass responsivity* of the cantilever which helps determine the minimum detectable mass of the device as,

$$\delta m^* \approx \Re^{-1}\delta f_0 \tag{2.7}$$

Equation 2.7 is based on the assumption that the additional mass is very small compared to that of the cantilever and the stiffness of the cantilever remains constant. It

suggests that the minimum detectable mass is a function of the material properties of the cantilever and the minimum detectable frequency shift that is bounded by the noise level [10, 11].

2.3 Additional Effect of Stiffness Change on Resonance Frequency

As described above, resonant mass sensing technique reported in the literature is based on the principle of relating the shift in the resonance frequency to the amount of adsorbate mass, *i.e.* the mass accumulated on the surface of the resonating cantilever beam, assuming the mass change only is responsible for this shift in resonance frequency. The major issue associated with this approach is the elimination or isolation of parameters other than mass that would also cause a shift in the resonance frequency. One major additional parameter is the change of stiffness induced by the accumulated material. The stiffness increases due to the increase in the total thickness after accretion and/or to the increase in the effective elastic modulus. Such an increase in stiffness would lead to a positive shift in the resonance frequency, while the accumulation of an additional mass on the resonating beam acts in the opposite way, as stated in the previous part of the chapter. Positive frequency shifts were reported for several experimental platforms including the selective placement of the bacteria Escherichia coli [12] or protein molecules [5, 7] and the case of water absorption by a gelatin coating [13], all on Si cantilevers. Hence, a theoretical treatment is necessary to isolate mass and stiffness effects.

In this part of the study, a bilayer Bernoulli beam model is adopted for the case of a uniform accretion of a material on the resonating cantilever beam, taking into account the effects of both the uniform bilayer (Ni/Au) structure of the micro-cantilevers and the integrated diffraction grating on the free end. Firstly, without the grating on the free end,

the resonance frequency of a bilayer Bernoulli beam with length L (assuming mass density of each layer constant, and using the relationship between the mass and thickness as well), is calculated as [14]

$$f_0 = \left(\frac{1.8751^2}{4\pi}\right)\frac{m_0}{\rho_0 A L^2}\sqrt{\frac{E_0}{3\rho_0}\frac{\left(\rho_r^4 + 4\rho_r^3 E_r m_r + 6\rho_r^2 E_r m_r^2 + 4\rho_r E_r m_r^3 + E_r^2 m_r^4\right)}{\left(1+m_r\right)\left(\rho_r + E_r m_r\right)\rho_r^3}} \qquad (2.8)$$

where m_0, ρ_0, E_0 are the resonator's mass, mass density, and elastic modulus, respectively, and m_r, ρ_r, E_r are the ratio's of the same parameters of the adsorbate to those of the resonator.

Similarly, assuming the grating part is a mass put near the end of the beam (with distance L from the support), the resonance frequency for the beam with the integrated diffraction grating becomes:

$$f_0 = \left(\frac{1.732}{4\pi}\right)\frac{m_0}{\rho_0 A L^2}\sqrt{\frac{E_0}{3\rho_0}\frac{\left(\rho_r^4 + 4\rho_r^3 E_r m_r + 6\rho_r^2 E_r m_r^2 + 4\rho_r E_r m_r^3 + E_r^2 m_r^4\right)}{\left(\frac{A_p}{wL} + 0.236\right)\left(1+m_r\right)\left(\rho_r + E_r m_r\right)\rho_r^3}} \qquad (2.9)$$

The parameters used here are shown in Figure 2.1, where A is the total surface area, E elastic modulus, L length of the beam, ρ mass density. The index p designates the pad on which the grating is formed; index *0* is for the substrate (Ni), index *1* for the adsorbate, index r for the ratio of the adsorbate to that of the substrate.

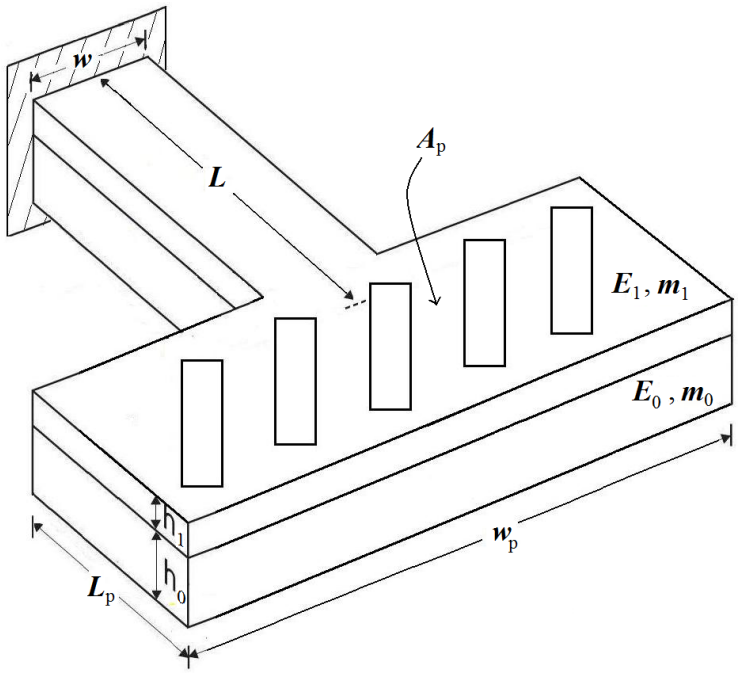

Figure 2.1. Depiction of the parameters used for the micro-cantilever modeling

The change in resonance frequency can be related to the change of mass through a first-order approximation to as,

$$\Delta f \approx \frac{\partial f}{\partial m}\Delta m = \Re \Delta m = \Re\left(E_0, \rho_0; E_r, \rho_r\right)\Delta m \tag{2.10}$$

where the proportionality constant, $\Re$, is again the mass responsivity, however, now taking the form (as a function of the material properties of the micro-cantilever sensor and the adsorbate mass as well):

$$\Re = \frac{f_0}{2m_0}\frac{\begin{pmatrix}-\rho_r^5+3\rho_r^4E_r+\left(12\rho_r^3E_r-2\rho_r^4E_r\right)m_r+\ldots\\ \left(6\rho_r^3E_r-4\rho_r^3E_r^2+12\rho_r^2E_r+6E_r^2\rho_r^2\right)m_r^2+\ldots\\ \left(8\rho_r^2E_r+12\rho_rE_r^2\right)m_r^3+\left(3E_r^3+7\rho_rE_r^2\right)m_r^4+2E_r^3m_r^5\end{pmatrix}}{\left(1+m_r\right)\left(\rho_r+E_rm_r\right)\begin{pmatrix}\rho_r^4+4\rho_r^3E_rm_r+6\rho_r^2E_rm_r^2+\ldots\\ 4\rho_rE_rm_r^3+E_r^2m_r^4\end{pmatrix}} \tag{2.11}$$

$$\approx \frac{f_0}{2m_0}\frac{-\rho_r+3E_r}{\rho_r} \quad \left(linearized\ for\ m_r \ll 0.01\right)$$

As both $\Re$ and its linearized form, for a very small amount of adsorbate mass, suggests, the shift in the resonance frequency is determined by not only the change in the amount of mass but also the change in stiffness induced by the elastic modulus of the adsorbate layer.

2.4 Theoretical Verification

The verification of the model is carried out first theoretically by considering two sample cases which make the isolation of these differing -stiffness and mass- effects of the absorbed material on a cantilever's resonance frequency, easier to visualize.

2.4.1 Sample Cases

The sample cases are chosen in such a way that one of these effects introduced by the adsorbed material is changed while the other is kept constant, and the consequent shift in the resonance frequency is observed. The differing effects of the change in stiffness and in mass on the shift in resonance frequency can, therefore, be shown separately.

Two samples are investigated in order to visualize these two competing effects on the resonance frequency. In the first sample, the effect of increasing ρ_r on the resonance frequency is observed for a fixed E_r. Therefore, in the second sample, the effect of increasing E_r on the resonance frequency is observed while this time ρ_r is kept constant.

2.4.2 Results

Figure 2.2 shows the effect of increasing ρ_r for a fixed E_r. The y-axis is the normalized frequency shift in the resonance frequency, while the x-axis is the normalized amount of adsorbed material. All normalization procedures are carried out with respect to those parameters of the cantilever.

The positive frequency shift in Figure 2.2a and b becomes negative as ρ_r is increased in Figure 2.2c. Three plots corresponding to the exact solution, first order approximation (R) and its linearized form, (R_l) are provided in each graph. The crosses (×'s) in both figures correspond to the finite element modeling results for corresponding parameters. Similarly, Figure 2.3 demonstrates the effect of increasing E_r for a fixed ρ_r. Here, the negative frequency shift in Figure 2.3a becomes positive when E_r is increased in b and c.

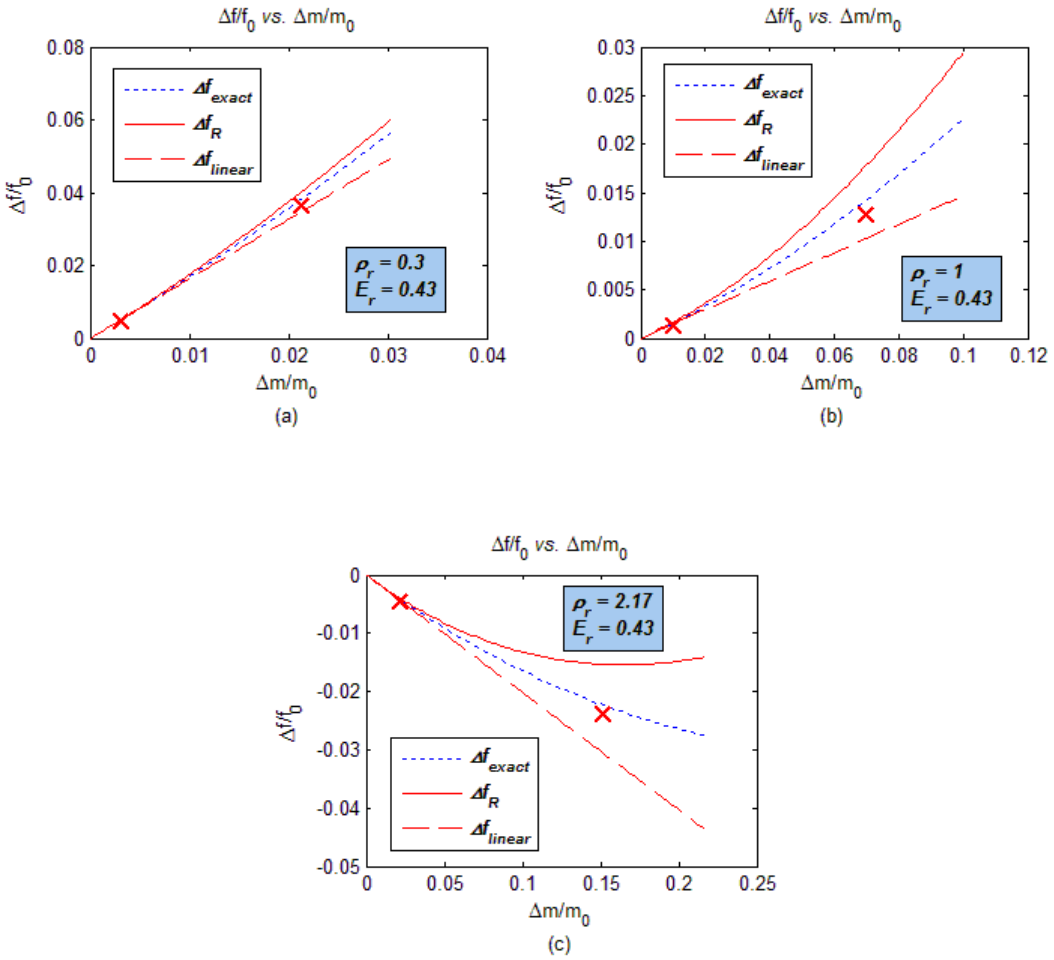

Figure 2.2: Dependence of the frequency shift on adsorbate mass density in the case of a constant ratio of elastic moduli. A switch from positive to negative shift takes place with increasing adsorbate mass density. (The ×'s indicate the finite element modeling results.)

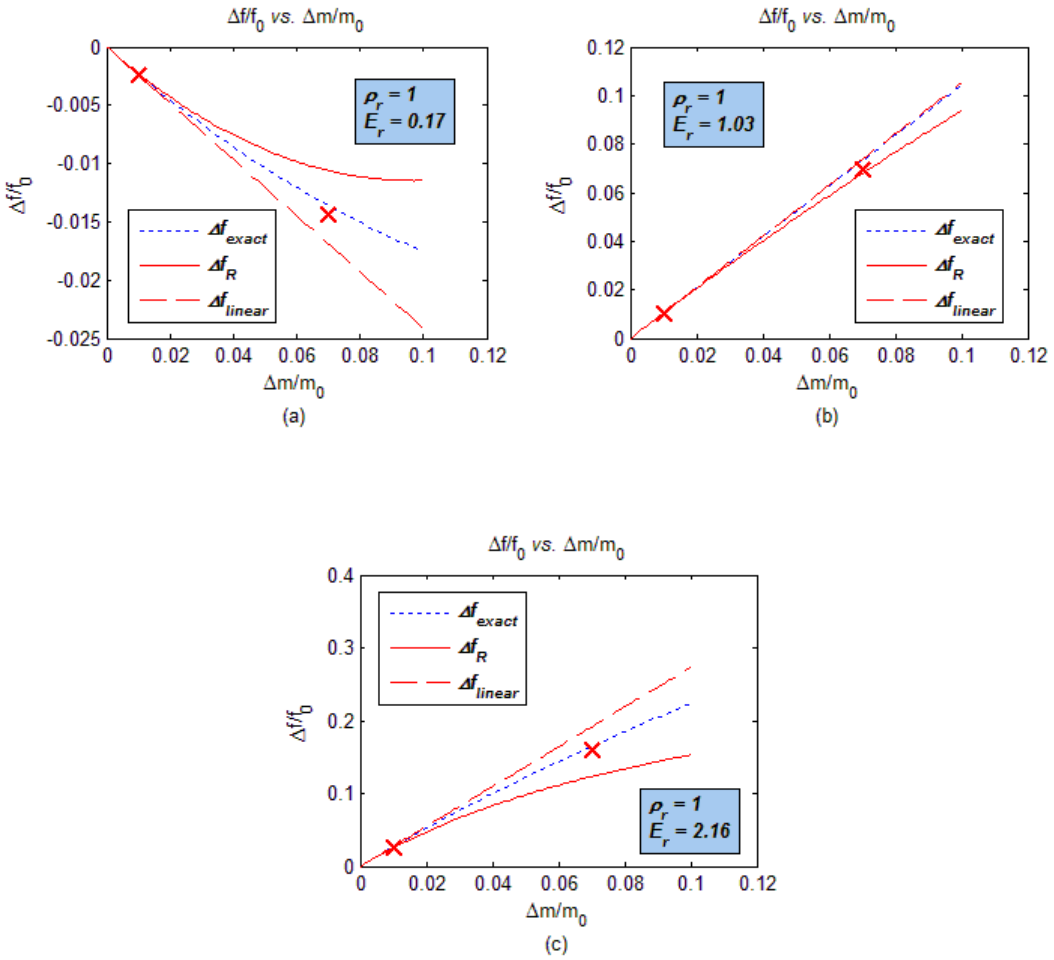

Figure 2.3: Dependence of the frequency shift on adsorbate elastic modulus in the case of same mass density of adsorbate and substrate. A switch from negative to positive shift takes place with increasing adsorbate elastic modulus. (The ×'s indicate the finite element modeling results.)

The graphs clearly indicate the competing effects of stiffness and mass on the resonant response of a cantilever. Therefore, the proposed model for the calculation of the shift in

the resonance frequency of a micro-cantilever beam due to adsorbed material, taking into account the stiffness change introduced by the adsorbate in addition to its mass, is theoretically verified.

2.5 Experimental Verification & Device Calibration

Although, the model is verified theoretically, an experimental validation, also, is necessary to show the validity and capability of the model. During the experiment the device is also calibrated in terms of the elastic moduli of its Ni and Au layers.

2.5.1 Experimental Setup & Procedure

In order to check the experimental validity of the model and obtain comparative experimental data by calculating a sample responsivity constant, a calibration experiment, which is described step by step, is designed and established successfully:

i. Firstly, the resonance frequencies of monolayer uniform Ni microcantilevers, of 2μm thick, 60μm length (integrated with 3 diffraction gratings of 3μm width and 6μm period), are measured.

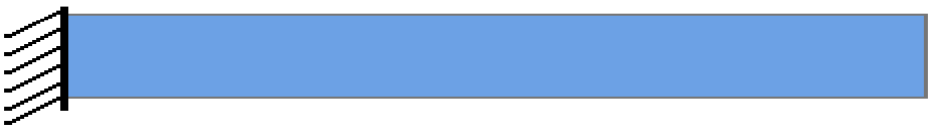

Figure 2.4 Schematic depiction of a monolayer uniform Ni microcantilever

ii. Setting out from these measurements, the device is calibrated for the Ni layer. (i.e.

the elastic modulus for the Ni layer is calculated: 112.53 ±2.27 GPa).

Figure 2.5 Schematic depiction of accumulation of a Au layer on top of a monolayer uniform Ni microcantilever

iii. On top of these cantilevers, a 482nm thick Au layer is deposited by RF magnetron sputtering method and the new resonance frequencis are measured.

Figure 2.6 Schematic depiction of the 1st incremental addition of Au layer on top of the initial bilayer uniform Ni-Au microcantilever

iv. The device is now calibrated for the Au layer. (i.e. the elastic modulus for the Au layer is calculated: 44.79 ±1.38 GPa).

Figure 2.7 Schematic depiction of the 2nd incremental addition of Au layer on top of the bilayer uniform Ni-Au microcantilever

v. Subsequently, in two separate sputter-deposition process, 30 and 40nm thick Au layers are deposited, respectively, and the resonance frequencies for both cases are

measured.

vi. The shift in the resonance frequencies caused by these last two depositions are compared with the theoretical calculations.

2.5.2 Results

The results of the experiment are compared with the expected/obtained theoretical calculations in Table 2.1. Here, "R_{theo}" columns are obtained using the shifts in the resonance frequencies, which are calculated by using, in equation 2.8, the amount of accumulated mass during the last two depositions; "R_{exp}" columns are obtained by using the frequency shifts measured during the last two depositions. Indices *1* and *2* express the states after the first and second depositions, respectively.

The values in the table indicate that the responsivities obtained using experimental results and the ones obtained from theoretical calculations are in good agreement. The ratios of the amount of the increases both in theoretical and experimental values after the second deposition process are also very close: R_{exp} has increased 12.54% while R_{theo} has increased 11.23%. It should be noted, that in all the tested cases, interestingly, though the mass is increased, the shift in resonance frequencies are positive and that the model could calculate this successfully.

Table 2.1: Responsivity Results

R_{theo1} *(Hz/pg)*	R_{exp1} *(Hz/pg)*	R_{theo2} *(Hz/pg)*	R_{exp2} *(Hz/pg)*
0.393	0.383	0.437	0.431
Error = 2.49%		*Error* = 1.35%	

$$R_{theo1} = \frac{\Delta f_{theo1}}{\Delta m_{exp1}} \qquad R_{exp1} = \frac{\Delta f_{exp1}}{\Delta m_{exp1}}$$

$$R_{theo2} = \frac{\Delta f_{theo2}}{\Delta m_{exp2}} \qquad R_{exp2} = \frac{\Delta f_{exp2}}{\Delta m_{exp2}}$$

Figure 2.8 The terms used in the interpretation of the results of the calibration experiment

Table 2.2: Calibration Results

	Elastic Modulus	Standard Deviation	Reported Values [15]	Reported Values [16]	Reported Values [17]	Reported Values [18]
Au (*GPa*)	44.79	±1.38	-	53-55	30-78	55
Ni (*GPa*)	112.53	±2.27	85-205	-	-	-

Apart from these results, the elastic moduli calculated for Ni and Au layers for device calibration are found to be in agreement with previously reported values for Ni [15] and for Au [16-18]. Calibration results and reported values are shown in Table 2.2.

2.6 Conclusion

The exact model, and a first order approximation to it, formulating the shift in resonance frequency of a uniform bi-layer Bernoulli cantilever beam as a function of both mass and stiffness (mainly the elastic modulus) of the adsorbate material, assumed to be a

second layer on the cantilever, is verified theoretically and experimentally with these results. The results obtained in the context of the theoretical examples exhibit, more visually, the competing effects of stiffness and mass changes on the shift in resonant frequency. In addition, these effects are observed within the experimental application (calibration) and the theoretical calculations, using the model, are found to be very close to the experimental results. Therefore, it is demonstrated, both theoretically and experimentally, to be more accurate to consider in micro-scale resonant mass sensing applications, that not only the mass change but the stiffness change induced by the accumulated mass, also, has a significant influence on the shift in resonance frequency, especially when this mass is accumulated as a uniform layer on the sensor cantilever. Using this generalized approach one can directly relate these resonance frequency shifts, which can be positive or negative, to the accumulated mass for any stiffness mismatch, which is very important for many bio-chemical sensor applications, where one has to deal with analytes accumulated along the surface of the sensor micro-cantilever, such as the case of this study. Also, in the course of the experimental verification, the (linear) responsivity of the micro-cantilever structure is shown to change due to successive addition of layers of the material (Au in this case) and can be calculated with this new model. This suggests that sensor devices with different functionalization/bio-sensing layers can have different responsivities, even when the bare micro-cantilever is exactly the same; i.e. the mechanical responsivity of a bare micro-cantilever beam, even if not totally irrelevant, is not enough to characterize it for bio-sensing applications.

Chapter 3

DEVICE FABRICATION

3.1 Fabrication Flow

Fabrication of the micro-cantilevers follows an earlier work reported in theses by Ocakli[2] and Ozturk[3] also in [19]. The process briefly consists of the following steps as shown in Figure 3.1: Substrate (Si-wafer) preparation, seed (Cr & Au) layer formation, mold-pattern preparation (UV Photolithography), micro-cantilever structure formation (nickel electro-deposition), releasing the micro-cantilevers (wet etching of secondary layers and deepening the substrate), and the final cleaning.

3.1.1 Substrate Preparation

Removal of any possible residual particles, such as dust, on the Si wafer before starting the fabrication of micro-cantilevers is a crucial step in the process due to the fact that the dimensions of such particles are significant that they can interfere with the process and the structures to be fabricated. Therefore, the Si wafer (with thickness 525±25 μm, and resistivity 0.1–0.5 Ωcm) is cleaned using a standard cleaning procedure, using acetone,

isopropyl alcohol and DI water, and blown dry with N_2 gas, so as to get rid of any such particles prior to further processes.

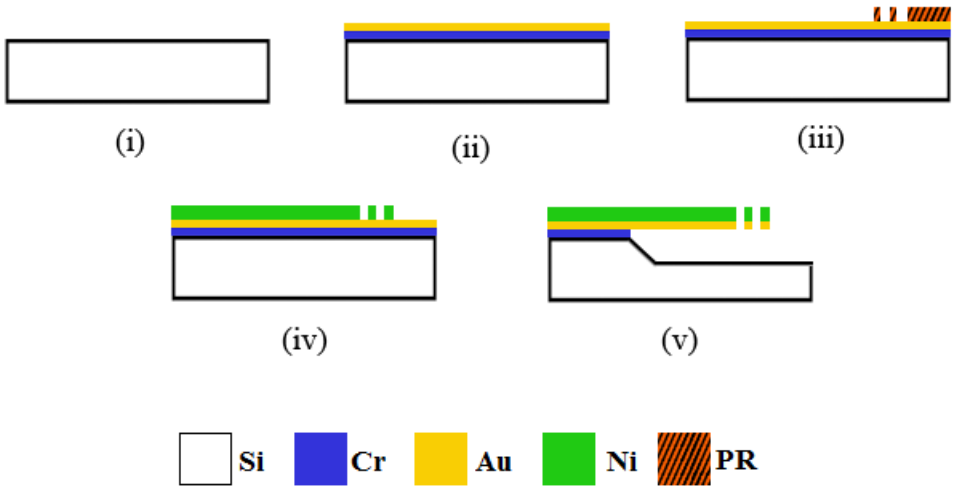

Figure 3.1 Fabrication Flow: (i) Substrate preparation, (ii) Seed (Cr & Au) layer formation, (iii) Mold-pattern preparation, (iv) Micro-cantilever structure formation, (v) Releasing & cleaning the micro-cantilevers.

3.1.2 Seed Layer Formation

The formation of the micro-cantilevers is done by electroplating, for which the electrical conductivity of the sole Si wafer does not suffice. In order to increase the conductivity of the substrate surface, coating a thin conductive layer is necessary, which has been chosen to be of gold (Au) for its high conductivity and potential to be functionalized as a bio-sensitive surface with appropriate receptor bio-molecules. Since there will be an adhesion problem between the Au and Si surfaces, a thin layer of

chromium (Cr) is also necessary. Both Cr (*10-20nm*) and Au (100-120nm) surfaces are sputter-deposited on the Si wafer utilizing an RF-Magnetron sputtering system.

3.1.3 Mold-Pattern Preparation: UV Photolithography

UV-photolithography is utilized to define the mold-pattern, which is to be filled as micro-cantilever structures. This UV-photolithography procedure starts with spin coating of a UV-sensitive mold material on the wafer surface. The wafer is then baked for 10min at 110ºC for better adhesion to the surface. After soft-bake, the wafer is exposed to UV light through the mask containing the predefined shapes of the micro-cantilever structures. The openings for the micro-cantilever electro-deposition are obtained by putting the wafer into the AZ 400K® developer solution.

The critical issues that specify the quality of pattern definition, such as the thickness of the resist, which depends on the UV-exposure time, development time and rate, were already improved as a good-working recipe in the study of Ocakli [2]. Briefly, resist thickness of 1.4-1.6μm is achieved suitably to obtain 1μm thick micro-cantilevers.

3.1.4 Micro-cantilever Structure Formation

Following the mold-patterning procedure, the whole wafer is sliced into dice and nickel micro-cantilever structures are electro-deposited onto the exposed Au surface on each die via electroplating using nickel-sulphamate bath [2, 3], consisting of 40 g/L H_3BO_3, 600 g/L $Ni(SO_3NH_2)_2.4H_2O$ and 10 g/L $NiCl_2.6H_2O$. A schematic of the bath and the electro-deposition process is shown in Figure 3.2.

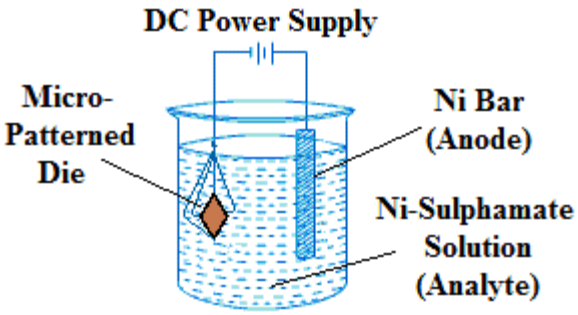

Figure 3.2 Electro-deposition process.

Adjusting current density, temperature and duration of the deposition, thickness and surface roughness of cantilevers can be controlled. During electroplating, current density of ~40mA/cm^2 is used. To achieve a homogenous and shiny deposition on the die (which is necessary for readout), electrical contact is established along four edges of a die and the deposition solution is continuously stirred. Since Young's modulus depends on temperature deposition temperature is set to ~45°C, to achieve highest modulus according to Luo et al [15].

3.1.5 Releasing the Micro-cantilevers: Wet Etch

After the cantilevers are obtained by electroplating, PR is removed by AZ 100® remover and exposed films of Au and Cr are etched consecutively in order for cantilevers to be released. Au is time-etched, using a commercial (Transene TFAC) Ni-selective Au etchant, in order to preserve Au layer underneath since it serves as functionalization layer for bio-recognition/detection. The presence of such a layer is later verified by scanning electron microscopy. Afterwards Cr is etched using a commercial (MicroChrome TFE) Cr etchant. Cantilevers are then completely released by anisotropic wet etching of Si layer with 35%

KOH solution at 65°C to optimize the roughness of Si surface and prevent stiction of the cantilevers. Higher temperatures are observed to result in stiction for most of the cantilevers on the chips. Etching is carried out to 10-20μm depth to avoid squeeze film damping effects [20]. At this step, it should be noted that the Ni layer serves as the etch mask for Si eliminating the need for another step of photolithography. Ni also shows high corrosion resistance, which is necessary for reliability in biosensor applications [3].

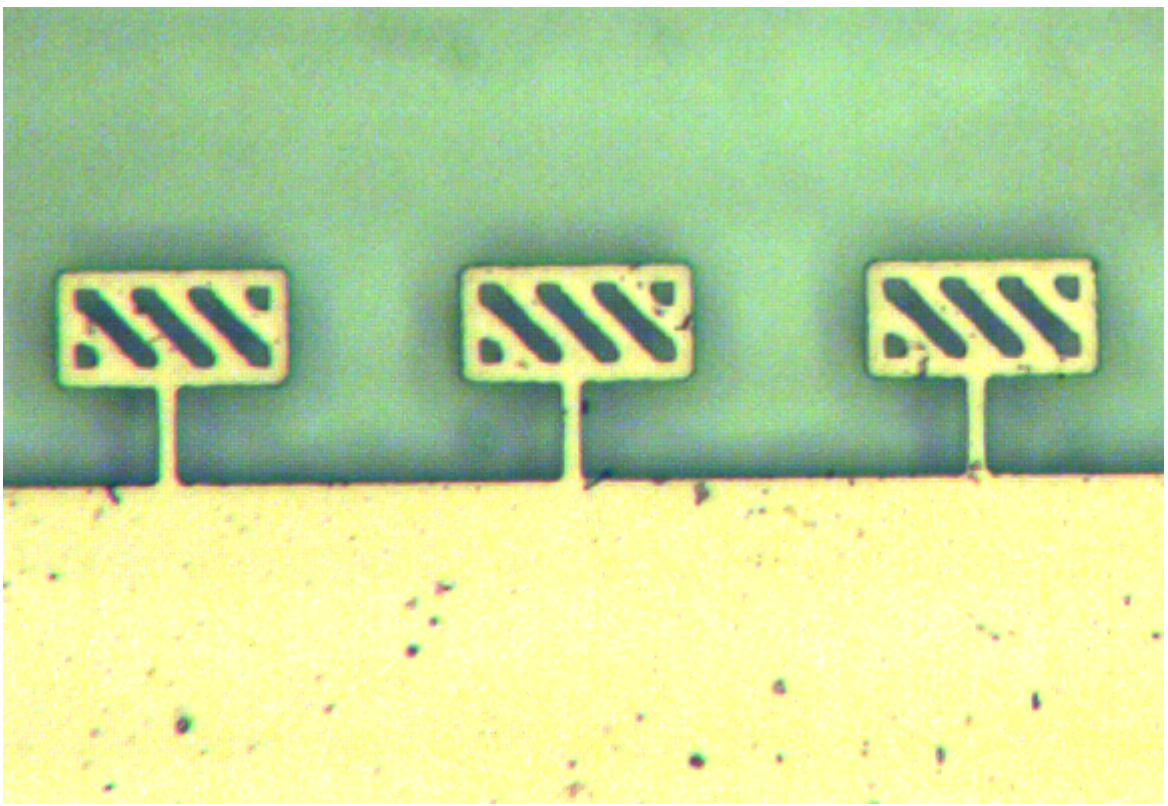

Figure 3.3 An array of micro-cantilevers that is ready for measurement.

After Si etch, the Cr layer underneath is removed completely, leaving the Au layer underneath exposed for later bio-functionalization. Figure 3.3 shows an array of micro-cantilevers ready for measurements.

3.1.6 Final Cleaning

After the cantilevers are successfully released, the die is RCA1 cleaned to remove any possible organic residues, especially, in order to ensure a clean Au surface for further functionalization. The method utilizes a treatment of the dice with a mixture of NH_4OH:H_2O_2:DI-water with the proportions 2:3:10 at around 70 °C for 10 minutes. After treatment, die is carefully DI-rinsed and dried simply by putting on the heater for a few seconds.

3.2 Encountered Problems

There were recipes for each of the processes developed by Ocakli[2] and Ozturk[3], however, some problems entailed during following processes and were solved accordingly.

3.2.1 Delamination Due to Crocodile Tips

As mentioned previously, the cantilever dice were connected along the four edges for deposition uniformity, using crocodiles. Since these crocodiles had an array of sharp tips, they used to tear the thin Au layer. These small tears in further etching processes initiated

delaminations on the edges increasing and consequently causing the Ni cantilever layer to strip-off very easily. In order to eliminate this problem the crocodiles were wrapped-up with pieces of aluminum foil preventing the sharp tips from tearing the Au layer.

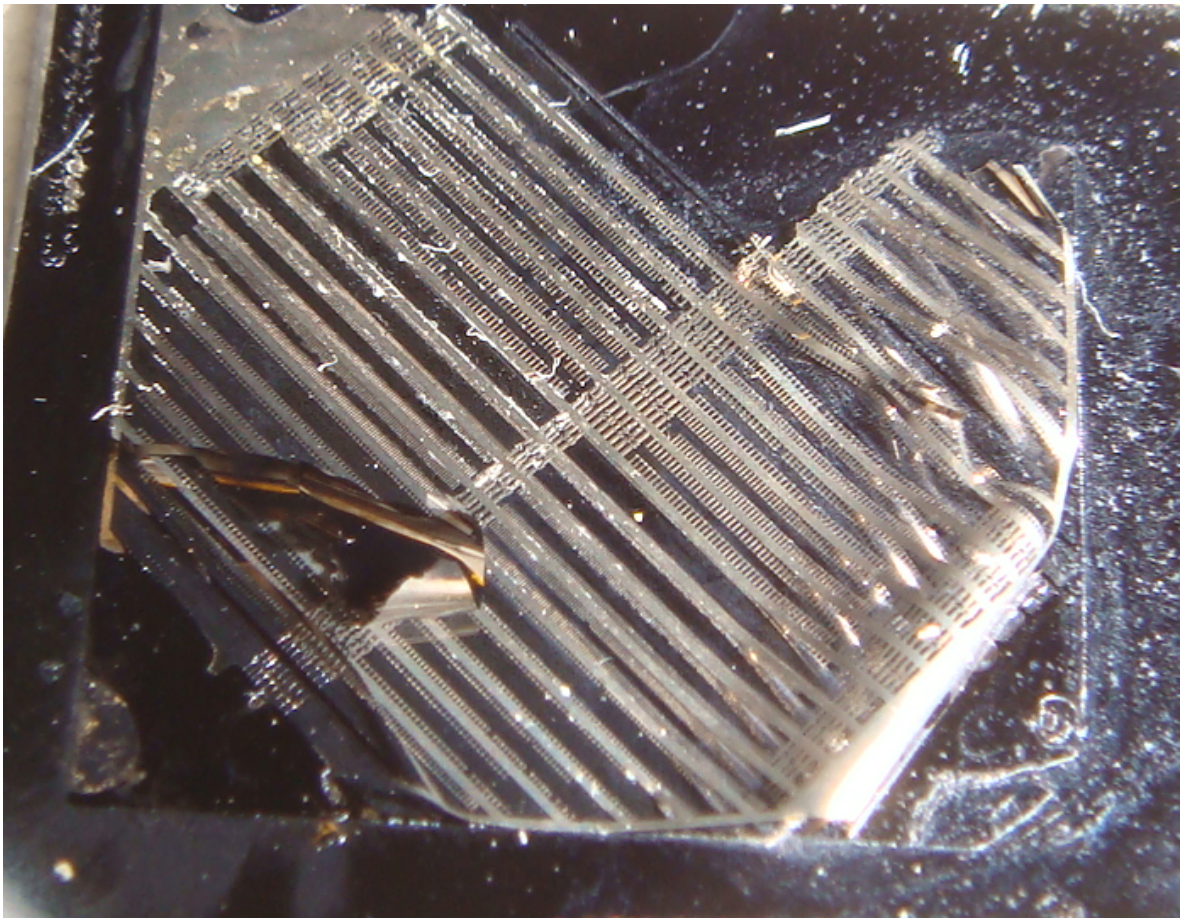

Figure 3.4 A sample die with the main structure is torn off due to delamination.

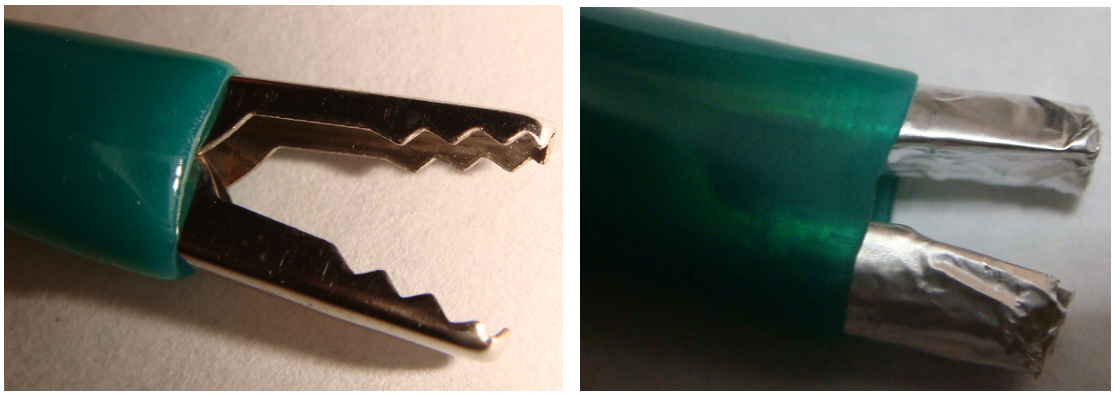

(a) (b)

Figure 3.5 A sample crocodile used for electrical contact during electro-deposition (a) before and (b) after covering with Al-folio.

3.2.2 Excessive Undercuts Due to Over-etched Cr & Au Layers

In the previous studies by Ocakli[2] and Ozturk[3] the Cr and Au etching processes were carried out harshly, since the timing was very tight: 10sec for Cr etch and 1min for Au etch. Since the layers upon the Si substrate serves as an etching mask for Si etch process, an uncontrolled etching of Au or especially Cr results in deeper going undercuts beneath the Ni anchor, preventing controllability of the cantilevers.

This excessive undercut problem was solved significantly, once Cr and Au layers were etched with lower concentrations of the same etchants (both with “etchant”:“DI-water” ratio of 1:3), therefore, in longer time intervals (around 1-2min for both etches).

3.2.3 Stiction Due to High Si Etch Rate

When the cantilevers were tried to release with Si etching at 70ºC as reported by Ocakli[2] and Ozturk[3], many lines of cantilevers, especially the longer ones, on every single die used to exhibit an unsystematic stiction problem, i.e. the cantilevers would not release most of the time. By trial and error, however, it was observed that almost all the cantilevers were released straight, once the etch rate was decreased by lowering the temperature down to 65ºC.

3.3 Conclusion

In this chapter, Device Fabrication, the fabrication flow and the solutions to some of the encountered problems, during the fabrication stage of the thesis, are briefly explained. Namely, the delamination, undercut and stiction problems are solved to improve for a faster and more efficient fabrication process.

Chapter 4

MEASUREMENT SETUP AND PROCEDURE

4.1 Actuation Setup

The actuation setup follows the study of Ozturk [3] with some modifications, which will be mentioned later in the chapter, to improve the readout signal quality. The Ni micro-cantilevers are actuated electromagnetically with an external electromagnetic coil. Cantilevers are sinusoidally excited at their first order resonance frequencies by a signal generator. The output signal is read out by a photo-detector diode (PD). The actuation and readout signals are monitored via an oscilloscope. A schematic description of the measurement setup is shown in Figure 4.1.

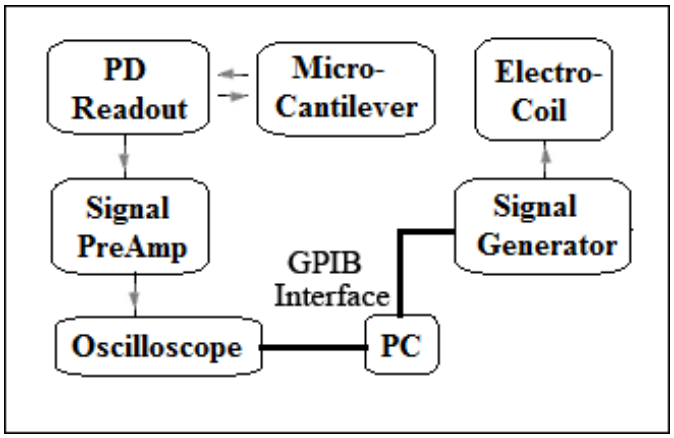

Figure 4.1: Schematic description of the measurement setup.

4.2 Photo-detector Setup

A photo-detector setup is built in order to utilize the grating interferometry. A photograph of the setup is shown in Figure 4.2.

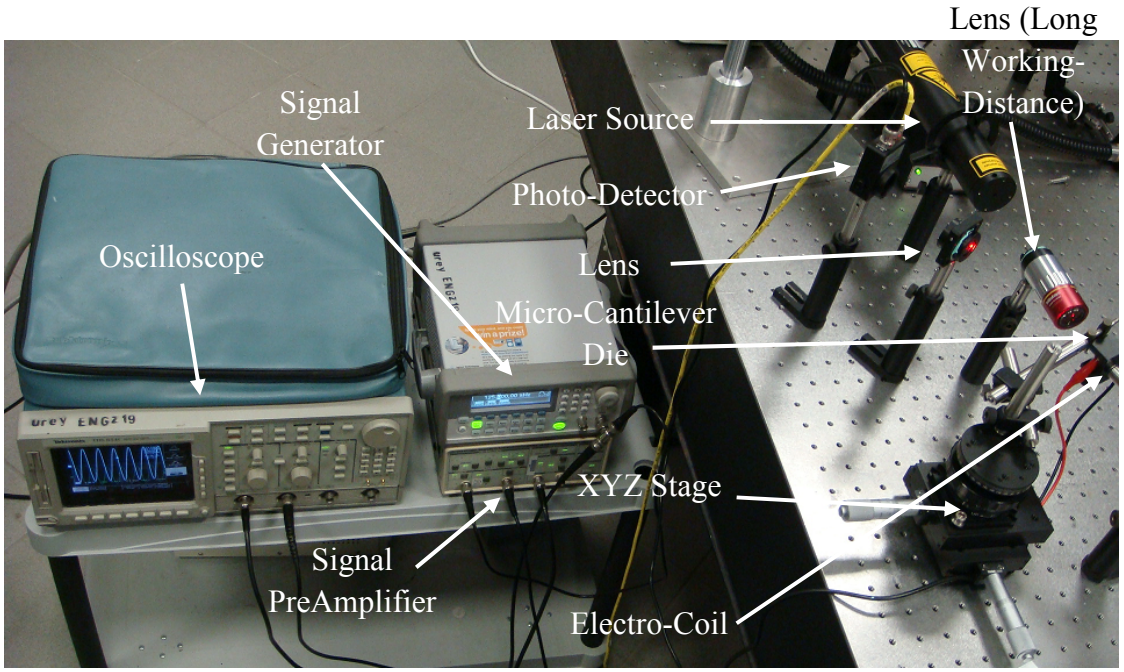

Figure 4.2 Measurement Setup

The operation of diffraction grating interferometric measurement is shown in Figure 4.3. The intensity of the light diffracted from the gratings modulates with a period of $\lambda/2$, where λ is the wavelength of the incident laser beam, as the gap between the cantilever and the substrate changes due to the sinusoidal deflection of the cantilevers when actuated.

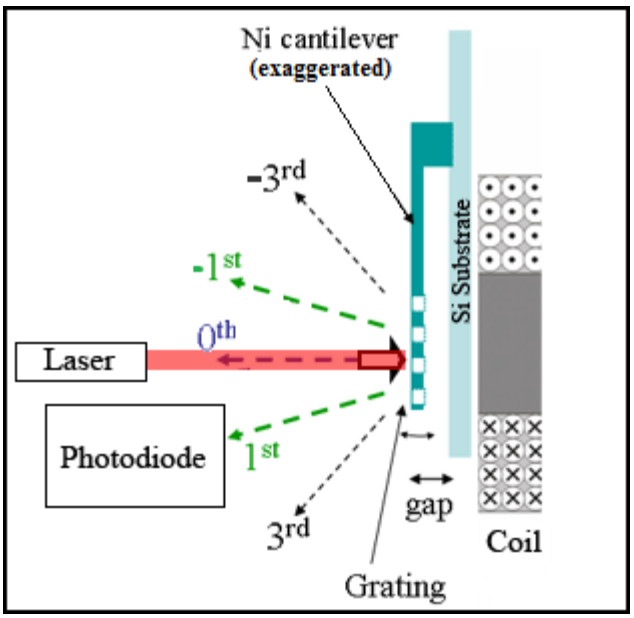

Figure 4.3: Optical readout with electromagnetic actuation. PD intensity is a sinusoidal function of the gap with a period of λ/2

The deflection of the cantilevers is observed by simply monitoring the sinusoidal intensity modulation. The actuation signal is swept across a range of frequencies and the readout signal amplitude (peak-to-peak) versus the frequency input (and output) signal is recorded, which gives out the frequency response curve, and therefore, the resonance frequency of the cantilevers. The resonance frequency and the Quality-factor, Q, is extracted using a Lorentzian-like nonlinear fit to the frequency response curve obtained from the readout signal. The frequency response curve of a sample micro-cantilever is shown in Figure 4.4.

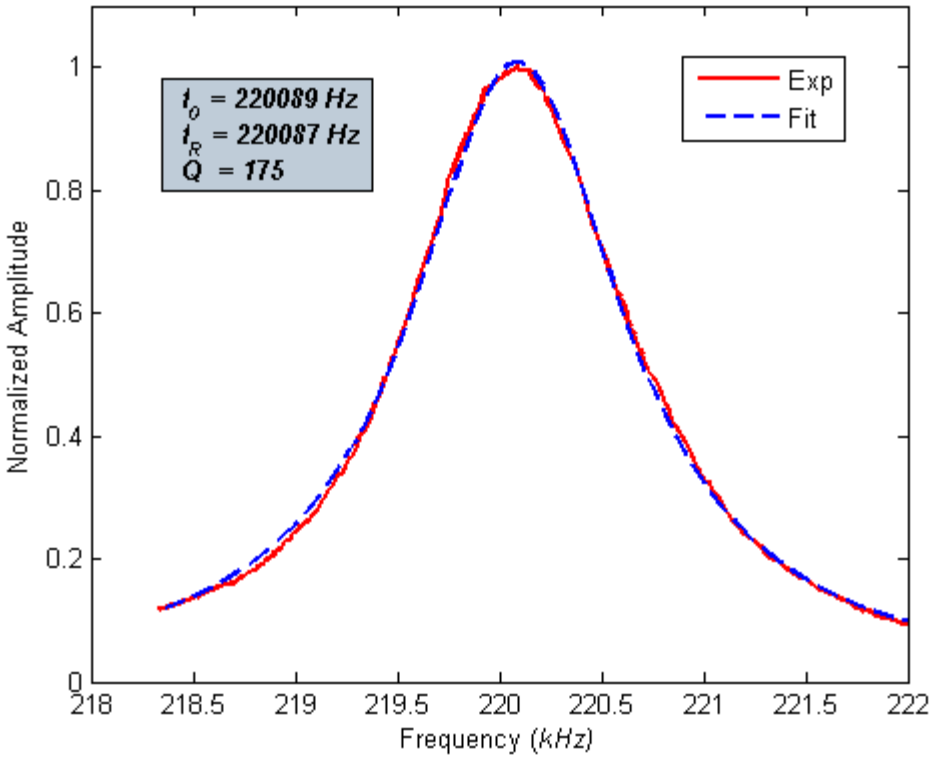

Figure 4.4: A sample response curve and the nonlinear fit with the parameters resonance frequency, f_0, and quality factor, Q, extracted.

The micro-cantilevers on the die are illuminated with a He-Ne laser of 633 nm wavelength. The 1st or 0th order of the diffracted light from the gratings is then focused on a wideband amplified Si photodiode. The photodiode output is monitored on the oscilloscope after it is amplified with a commercial (Stanford Research Systems SR560) preamplifier. The cantilevers are oscillated within a range of frequencies with the signal generator, which is automated using a computer program through a GPIB interface.

4.3 Noise Immunity of the Setup

A simple experiment is designed to qualitatively test the noise immunity of the diffraction grating interferometric readout method. The experiment setup is shown in Figure 4.5.

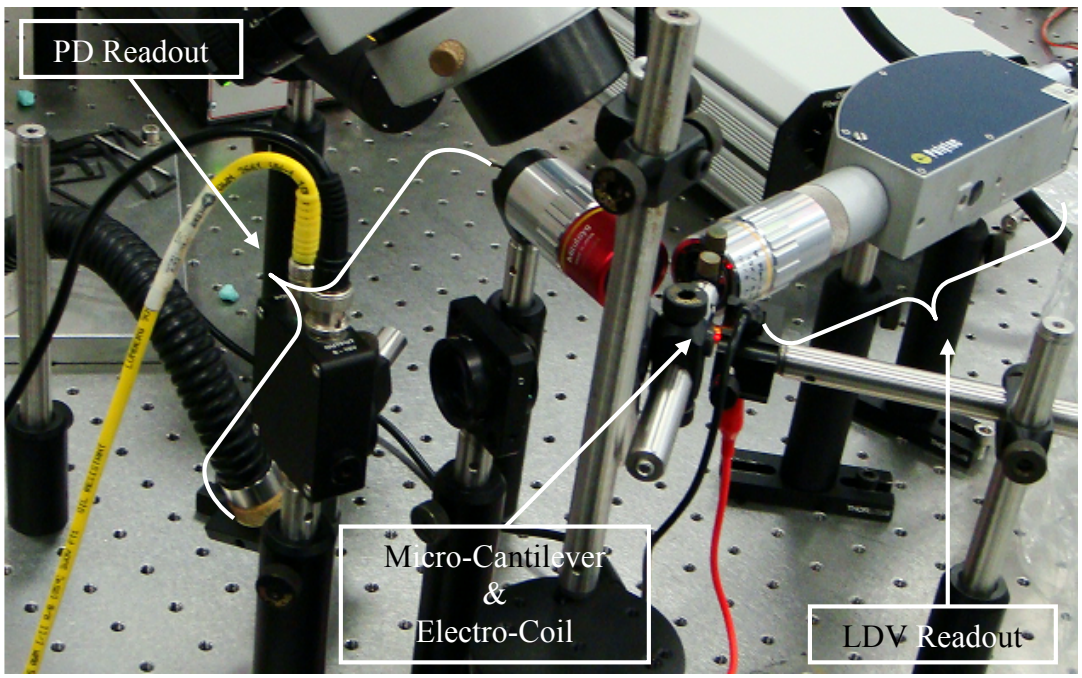

Figure 4.5 PD vs LDV noise immunity comparison setup

Briefly the PD measurements are compared with the readings of a commercial Laser Doppler Vibrometer (LDV) (Polytec OFV-2500 with a bandwidth of 0,5 Hz – 1.5MHz). The measurements are using the same micro-cantilevers in presence of a mechanical noise source. Although the resonance frequencies found both by LDV and PD measurements

seem to be the same, there is a significant difference regarding their responses to the presence of the same noise source. Previously, it was reported by Ozturk that the noise in both measurements with PD and LDV were the same however, instead of doing measurements in presence of a noise source, the reported LDV measurements were done with vibration isolation, significantly eliminating the mechanical noise. Even those measurements, also, show a higher robustness for PD measurements, since no clear resonance curves were reported to have obtained by LDV without vibration isolation; however, comparing the noise characteristics of two different setups should be carried out within the same environmental conditions for both setups. Figure 4.6 shows the comparison results of for a specific cantilever of width 12µm and length 60µm.

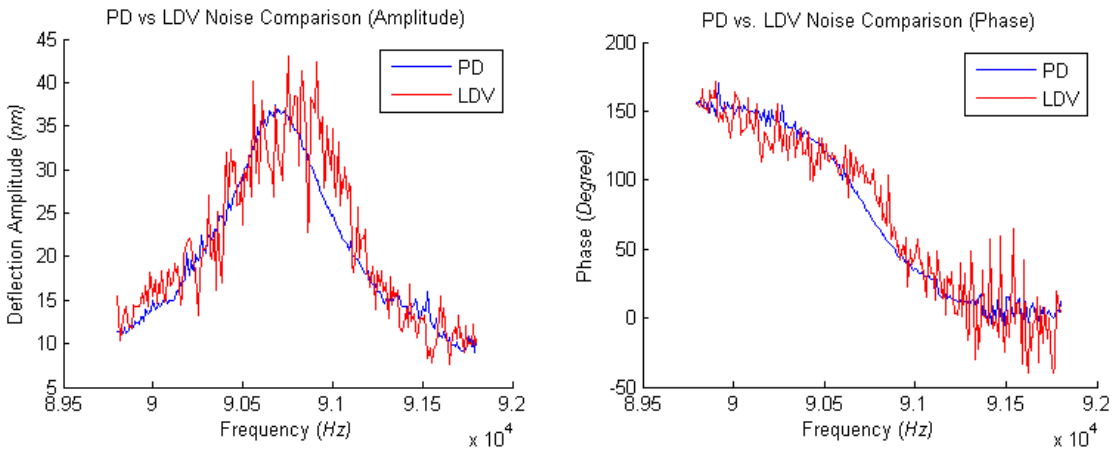

(a) (b)

Figure 4.6 Comparison of PD and LDV measurements for a cantilever of dimensions 12µm × 60µm in the presence of the same mechanical noise source: (a) Amplitude plot, (b) Phase plot of the frequency responses of PD (blue) and LDV (red) measurements

4.4 Improvements on the Setup

The measurement setup, also, had some noise problems due to some components used in the setup reported by Ozturk [3].

4.4.1 Removal of the Current Amplifier

The current amplifier utilized previously in the setup was especially effective for high frequencies around 500kHz. However, for lower frequencies the amplifier used to behave as a noise source, especially at resonance frequencies, whether because of the circuitry inside or the relatively high (~1.5x) current output causing the cantilevers to deflect in a range more than half the wavelength of the laser. Since the resonance frequencies that were studied did not exceed around 250kHz, the removal of the current amplifier did not change much in the actuation amplitude. Nevertheless, a significant improvement was achieved noise-wise. Therefore, the current amplifier needs to be improved or totally eliminated for better measurements.

4.4.2 Signal Amplitude

Even though the signal amplitude, without using the current amplifier, was high enough to observe, around resonance frequencies of the cantilevers, the amplitudes at off-resonance ranges, which were included to have a much better fit, dropped causing unclear resonance frequencies. Therefore, a commercial signal amplifier (SR560) was used to amplify the readout signal, especially for off-resonance frequency regions.

4.4.3 Laser Spot Size

Since the previous lens system used to focus the laser beam onto micro-cantilevers used to illuminate more than one cantilever, it was mostly hard to confidently observe the resonance frequency, especially that of the cantilevers that were closer to each other. Therefore, a new 10x lens with a long working-distance is used to focus the laser beam onto the cantilevers.

4.4.4 Determination of the Resonance Frequency

Previously, the resonance frequencies were determined by simply trying to observe the frequency where the maximum amplitude is read. However, especially for low-Q cantilevers/measurements, and the Q-factors observed were not that high, it will not be reliably accurate and precise to obtain the resonance frequency by this method. Therefore, a Lorentzian-like nonlinear fit to the resonance curves is utilized to extract the resonance frequencies. Figure 4.7 shows a sample measurement with fitted parameters and the percentage errors within the desired confidence interval, in this case 95%. As can be seen from Figure 4.7, the required parameters, resonance frequency, f_0, and Q-factor, are calculated easily and more accurately up to desired precision (within a given confidence interval).

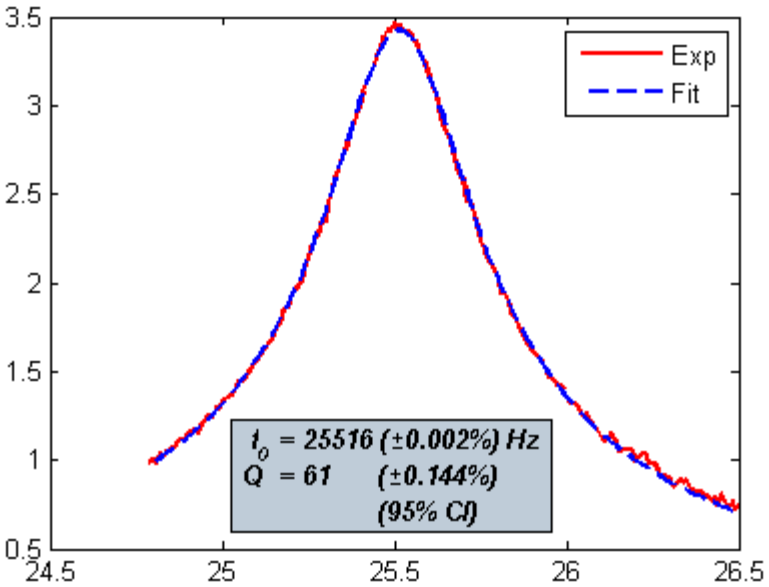

Figure 4.7 A sample measurement with fitted parameters and the percentage errors within 95% confidence interval

4.4.5 Higher-Order Modes of Resonance Frequency

One of the required parameters, mentioned by Ocakli[2], for higher sensitivities and responsivities is a higher resonance frequency. In addition to the high frequency of the higher resonance modes, they exhibit higher Q-factors also. Therefore, one can use higher-order resonance modes of the same sensor device, in order to improve its sensitivity and responsivity to the mass to be measured. The six plots in Figure 4.8 show resonance curves for the first three modes of the same micro-cantilever both in air and in water as a liquid environment.

In these measurements, the current decreases significantly due to the structure of the electro-coil, as the frequency is increased. Therefore, the deflection amplitudes measured for higher resonance modes are much less than the values they would be for the same amount of applied current at all modes (hence, the magnitude of the resulting electromagnetic field).

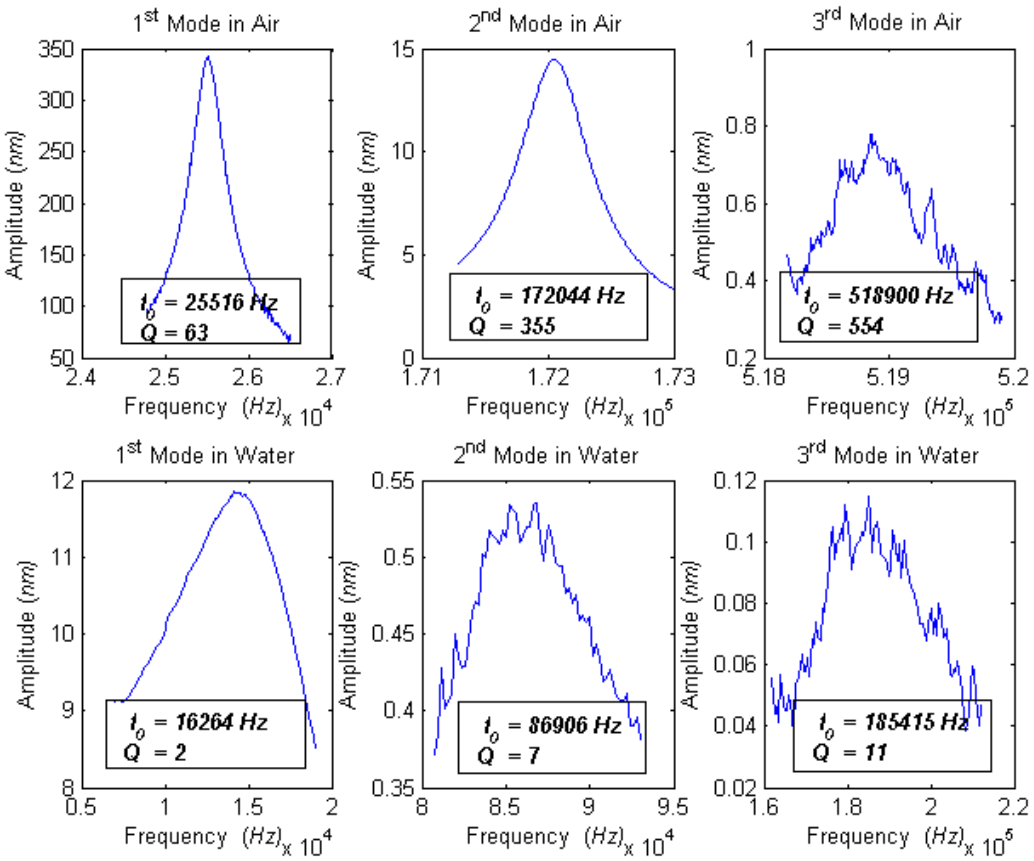

Figure 4.8 The first three resonance modes of a sample cantilever, both in air and in water. (*Note the sub-nanometer vibration amplitudes for 2nd and 3rd order resonance frequencies.*)

4.5 Measurement Procedure

As the main motivation of this study, human κ–opioid receptors (hKOR), which are selectively functional to narcotics molecules, were attached on the Au surface underneath the Ni cantilevers with the same biological techniques reported by Ozturk[3], so as to selectively detect this protein-antibody interaction. Instead of actual ligands, however, hKOR-antibody proteins were used in all the experiments as drug-simulant molecules. The shifts in resonance frequencies due to the bio-chemical accretion of protein molecules on cantilevers were observed for two separate processes: 1) Binding of (receptor) hKOR molecules to the cantilevers, 2) Binding of hKOR-antibody molecules to the receptor molecules. To demonstrate the sensor's selectivity to drug molecules 3 chips including cantilevers with the same width-to-length aspect ratio (1:5) are prepared. 11 cantilevers per chip are used for the measurements. After the initial resonance frequencies of the cantilevers were measured, one of the chips was functionalized with the method discussed above where another was functionalized with BSA, which has no affinity to hKOR-antibody. The third one was used as a reference/calibration chip to compensate the possible background effects during the bio-chemical treatment procedure.

Table 4.1: Summarized Treatment and Measurement Protocol

Step #	Process	Chip: Reference	Chip: hKOR	Chip: BSA
0	Fabrication	*	*	*
1	Protein (Receptor) Binding	-	hKOR	BSA
2	Antibody Binding	-	+	+

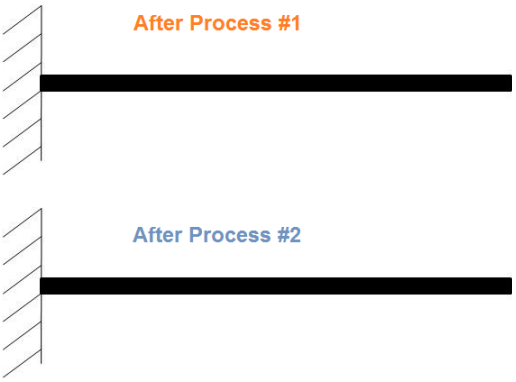

(a)

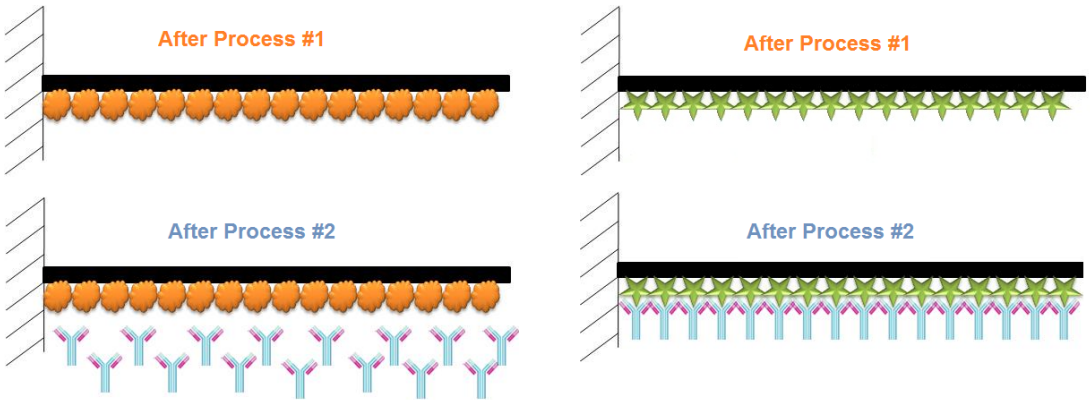

(b) (c)

Figure 4.9 The expected conditions of the cantilevers on the (a) Reference, (b) BSA, (c) hKOR chips after 1st and 2nd processes.

Following the functionalization of the cantilevers, all of the three chips are exposed to hKOR-antibody molecules and the resonant characteristics are observed as shown in the summarized protocol presented in Table 4.1. The +'s and –'s, in Table 4.1, represent the

presence and absence, respectively, of the related proteins in the analyte solutions; *'s mean no biological treatment is done before measurement. Before the measurements after each biological treatment process, the chips were dried under ambient conditions to measure the frequencies in air. The expected conditions of the cantilevers on these three chips after 1st and 2nd processes are depicted schematically in Figure 4.9.

The results and calculations for these measurements are presented and discussed in Chapter 5, Results & Discussions.

4.6 Conclusion

In this chapter, the improvements are briefly explained which are introduced in the setups that are used for actuacting the micro-cantilevers and for photo-detecting the signal corresponding to the vibration of these microcantilevers. Furthermore, it is qualitatively shown that photo-detecting by means of diffraction grating interferometric method has a much more immune behaviour in response to the environmental noise than measurements done by LDV.

Finally, the measurement procedure, which is followed to accomplish the selective detection of the protein-antibody interaction, is explained.

Chapter 5

RESULTS & DISCUSSION

5.1 Fabrication Process Variations

There are many parameters during the fabrication processes, which can affect the overall micro-mechanical properties of the micro-cantilevers. These parameters include, but are not limited to, the UV exposure duration, development time and profile of the photoresist mold-pattern, the electroplating duration and current density used for electroplating, uniformity of the electroplated Ni thickness, and so forth. The micro-mechanical properties are therefore affected by the variations in such parameters.

The variations in some major micro-mechanical properties of the microcantilevers, which are separately utilized in model verification and selective bio-detection experiments, are tabulated in tables Table 5.1-4. In Table 5.1, Ni thickness, resonance frequencies, and, both Ni and Au moduli (and their variations in terms of standard deviations) for the microcantilevers used in the experimental verification of the theoretical model are given; whereas in tables Table 5.2-4, the variations in these parameters for the reference, protein, and control dice, respectively, are provided.

Table 5.1 Fabrication Process Variations for Experimental Verification of the Theoretical Model

Cantilever #	Ni Thickness* (μm)	Frequency (Hz)	Ni Modulus (GPa)	Au Modulus (GPa)
1	1.931	102700	116.11	45.87
2	1.950	102470	113.31	46.67
3	1.924	101820	114.88	46.06
4	1.916	100740	113.48	45.80
5	1.877	97850	111.56	46.26
6	1.866	98650	114.73	45.71
7	1.878	97600	110.87	44.40
8	1.882	98410	112.20	44.72
9	1.893	98530	111.17	45.31
10	1.873	98600	113.72	45.13
11	1.764	93460	115.14	43.62
12	1.755	91140	110.67	44.11
13	1.762	90480	108.16	42.21
14	1.762	90900	109.21	42.37
15	1.764	92470	112.72	43.54
Average	1.853	97055	112.529	44.785
Std. Dev.	±0.071	±4288	±2.271	±1.383

*Thickness of the initial Au layer is 482nm.

Table 5.2 Fabrication Process Variations for the Reference Die
(Selective Detection of Protein-Antibody Interaction)

Cantilever #	Ni Thickness* (μm)	Ni Modulus** (GPa)	Frequency (Hz)
1	1.030	113.80	142275
2	1.063	118.89	140393
3	1.129	105.31	142383
4	1.145	102.50	143014
5	1.164	110.33	143622
6	1.115	110.81	143697
7	0.964	123.26	139919
8	0.966	125.44	138045
9	0.974	126.04	139534
10	0.975	125.55	139569
11	0.982	128.46	142027
Average	1.046	117.31	141316
Std. Dev.	±0.080	±9.16	±1902

*Thickness of the Au layer is 100nm.

** Au Modulus is assumed 45GPa.

Table 5.3 Fabrication Process Variations for the Protein Die
(Selective Detection of Protein-Antibody Interaction)

Cantilever #	Ni Thickness* (μm)	Ni Modulus** (GPa)	Frequency (Hz)
1	1.040	112.68	83238
2	1.036	110.21	82053
3	1.044	108.37	82161
4	1.047	111.01	83324
5	1.053	110.12	83537
6	0.994	109.98	78239
7	0.999	108.84	78298
8	0.990	112.41	78597
9	0.994	104.35	76484
10	0.987	106.10	76425
11	0.989	108.45	77354
Average	1.016	109.32	79974
Std. Dev.	±0.028	±2.50	±2882

*Thickness of the Au layer is 100nm.

** Au Modulus is assumed 45GPa.

Table 5.4 Fabrication Process Variations for the Control Die
(Selective Detection of Protein-Antibody Interaction)

Cantilever #	Ni Thickness* (μm)	Ni Modulus** (GPa)	Frequency (Hz)
1	1.099	107.12	97822
2	1.078	120.37	100841
3	1.066	119.37	99211
4	1.065	116.52	98021
5	1.073	118.19	99509
6	1.086	121.38	102064
7	1.031	125.04	97446
8	1.019	125.65	96437
9	1.019	120.11	94507
10	1.009	123.85	94760
11	1.011	125.20	95356
Average	1.051	120.25	97816
Std. Dev.	±0.033	±5.31	±2458

*Thickness of the Au layer is 100nm.

** Au Modulus is assumed 45GPa

5.2 Selective Detection of Protein-Antibody Interaction

The results for the protein-antibody interaction experiment are shown in Figure 5.1 and Table 5.5. In Table 5.5, the average normalized frequency shifts of the cantilevers are given with corresponding standard deviations. The indices correspond to the process numbers given in Table 4.1. Both in Figure 5.1 and Table 5.5, $\left.\frac{\Delta f}{f_0}\right|_{0\to 1} = \frac{f_1 - f_0}{f_0}$ represents the shift in the resonance frequency of a cantilever after the first process normalized with the initial resonance frequency. For the protein die, this normalized shift corresponds to a frequency shift due to hKOR attachment on to the micro-cantilevers and for the control die due to BSA attachment. Similarly, $\left.\frac{\Delta f}{f_0}\right|_{0\to 2} = \frac{f_2 - f_0}{f_0}$ represents the frequency shift of the cantilever after the second process; where f_0 is the initial resonance frequency, f_1 and f_2 are the resonance frequencies after the first and second processes, respectively. This normalized shift for the protein die this corresponds to a frequency shift due to the hKOR-antibody attachment to the hKOR proteins on the micro-cantilevers, whereas, for the control die, should correspond to the same shift observed after the first process. In Figure 5.1, the histograms for each die, before and after each process, are given with schematics of the corresponding cantilevers representing the processes. In Table 5.5, the average and the standard deviations (SD) of the normalized shifts in the resonance frequencies for the hKOR die are presented in the Protein column, and those for the BSA die are shown in the Control column.

In Figure 5.1a, the reference die results show an average positive shift after the first process, in which the die is introduced into the protein solution. There is no change after the die is exposed to antibodies during the second process. Since the measurements were

carried out in air, the positive shift after the first process might be due to mass accumulation during the drying process of the buffer.

In Figure 5.1b, the negative control die exhibits an average negative shift indicating an increase in mass after BSA functionalization, which is to prevent hKOR-antibody detection for this die. In fact, once exposed to hKOR-antibodies, the die undergoes an insignificantly small shift. The fact that there is no frequency shift upon exposure to antibodies is an indication of missing affinity of the control surface to antibodies.

Finally, Figure 5.1c shows the results for the protein die, which is expected to detect hKOR-antibody interaction. After the die is functionalized with hKOR proteins, it exhibits a negative shift, comparable to the control die. A negative shift larger in magnitude, as expected, occurred, following the hKOR-antibody exposure. This is expected since there should be an accumulated mass of antibodies attached to the hKOR proteins, indicating the affinity of hKOR protein molecules to the antibodies. This second negative shift observed for the protein die, which is significantly distinct from the first one, demonstrates the bio-selective detection, together with that the second shift observed for the control die is almost the same with its first shift.

Using these measurement results, one can calculate the average mass and surface mass density of the biological material adsorbed on the cantilever from the following. Assuming the change in elastic modulus of the cantilever is negligible, or the changes induced by a probable layer formed by only the bio-chemical solution (reference die) are close to that of the protein layer (hKOR and BSA dice) one can write,

$$\left\langle \frac{\Delta f}{f_0} \right\rangle = -\frac{1}{2}\left\langle \frac{\Delta m}{m_0} \right\rangle = -\frac{1}{2}\left\langle \frac{\rho_b t_b A}{\rho_0 t_0 A} \right\rangle = -\frac{1}{2}\frac{\sigma_b}{\rho_0}\left\langle \frac{1}{t_0} \right\rangle \quad (5.1),$$

where ρ and t are the volume mass density and thickness of the layers with subscript "*b*" for the biological layer and subscript "*0*" for the bare resonator. σ is the surface mass density of the additional layer with superscript *prot* standing for either the BSA or the hKOR die and *ref* standing for the reference die. f_0 is the initial resonance frequency of cantilever with Δf being the shift in this frequency.

Table 5.5 Average Shifts and Standard Deviations in Resonance Frequencies for Protein and Control Dice

	Protein		Control	
	Average	SD	Average	SD
$\left.\frac{\Delta f}{f_0}\right\|_{0\to1}$	-5.14 x10^{-3}	3.78x10^{-3}	-4.02x10^{-3}	3.45x10^{-3}
$\left.\frac{\Delta f}{f_0}\right\|_{0\to2}$	-6.54x10^{-3}	4.18x10^{-3}	-3.99x10^{-3}	3.84x10^{-3}

Hence, the surface mass density of the adsorbed is obtained as,

$$\sigma_b = \sigma_b^{prot} - \sigma^{ref} = -2\rho_0\left(\left\langle \frac{\Delta f}{f_0} \right\rangle_{prot} - \left\langle \frac{\Delta f}{f_0} \right\rangle_{ref}\right) \Big/ \left\langle \frac{1}{t_0} \right\rangle \quad (5.2).$$

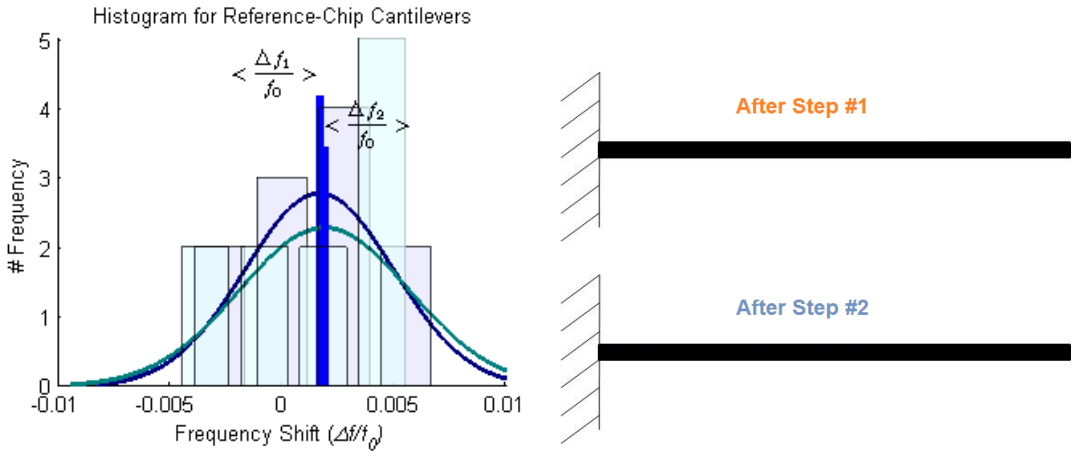
Histogram for Reference-Chip Cantilevers
Frequency
Frequency Shift ($\Delta f/f_0$)
$< \frac{\Delta f_1}{f_0} >$
$< \frac{\Delta f_2}{f_0} >$
After Step #1
After Step #2

(a)

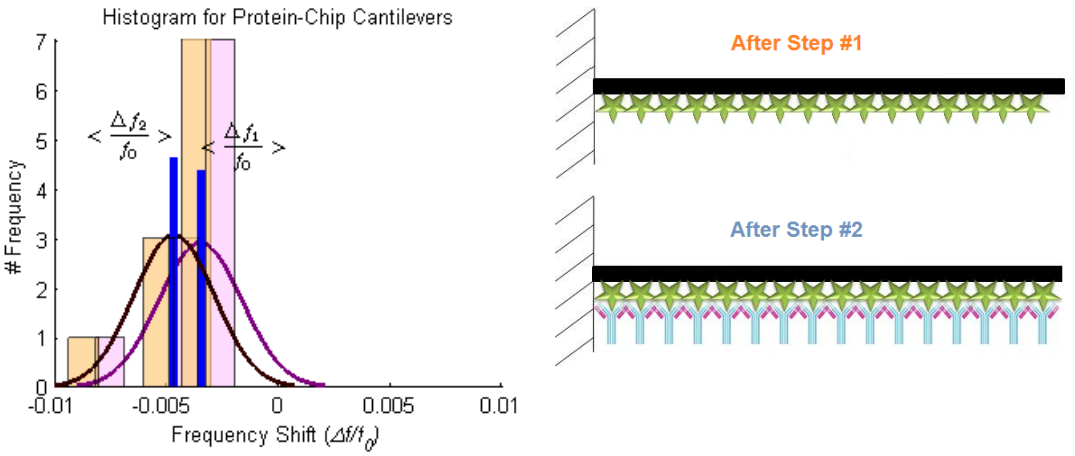
Histogram for Protein-Chip Cantilevers
Frequency
Frequency Shift ($\Delta f/f_0$)
$< \frac{\Delta f_2}{f_0} >$
$< \frac{\Delta f_1}{f_0} >$
After Step #1
After Step #2

(b)

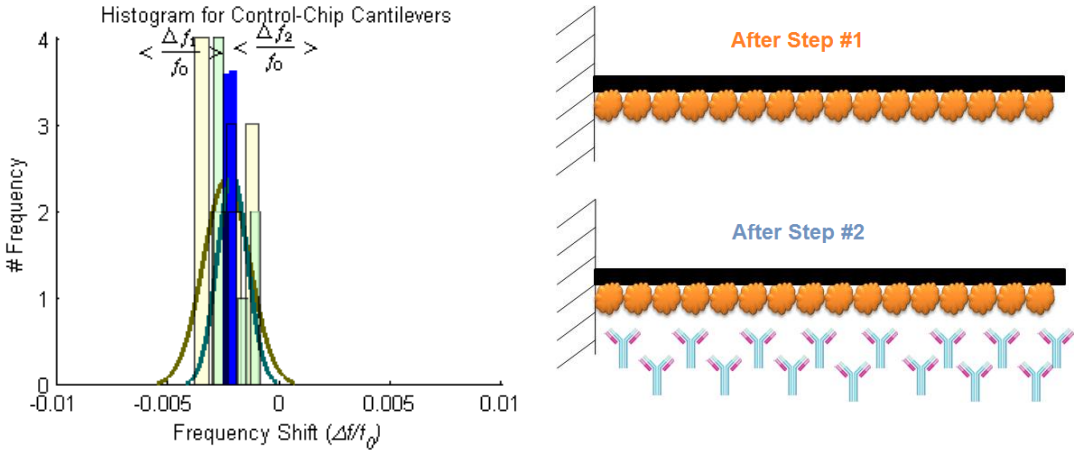

(c)

Figure 5.1: The average shifts in resonance frequencies of the cantilevers in three dice subjected to the procedure explained and the resulting cantilever depiction after the biochemical treatment corresponding to each die.

The resulting masses and surface mass densities of the detected biological materials, $\sigma_{measured}$, with corresponding values expected for the Control (BSA) and Protein (hKOR) dice, $\sigma_{expected}$, were calculated and shown in Table 5.6. These expected values were calculated using molecular masses of BSA (69kDa), hKOR (85kDa) and the hKOR-antibody (160kDa) proteins and the surface areas occupied by these molecules, 16.0nm^2 (BSA), 19.6nm^2 (hKOR and hKOR-antibody). Since the size of the antibodies are about 4 times larger than the hKOR proteins and they tend bind askew sidelong to the proteins, it was assumed, for the 2nd process, that only one-sixth/seventh of the hKOR-antibodies could bind to receptor hKOR proteins at maximum.

Table 5.6: Expected and Observed Surface Mass Densities for Protein and Control Dice

		Process #1	Process #2
Control	$\sigma_{measured}$ $(pg/\mu m^2)$	8.90×10^{-2}	8.82×10^{-2}
	on cantilever *(pg)*	93.31	92.43
	$\sigma_{expected}$ $(pg/\mu m^2)$	7.16×10^{-3}	7.16×10^{-3}
	on cantilever *(pg)*	7.51	7.51
Protein	$\sigma_{measured}$ $(pg/\mu m^2)$	1.14×10^{-1}	1.45×10^{-1}
	on cantilever *(pg)*	128.81	163.92
	$\sigma_{expected}$ $(pg/\mu m^2)$	7.19×10^{-3}	$9.13 - 9.45 \times 10^{-3}$
	on cantilever *(pg)*	8.15	10.34 - 10.71

An additional mass with surface mass density, $\sigma_{measured}$, $8.90 \times 10^{-2} pg/\mu m^2$, is observed on the cantilevers in the control die after the 1st process, however, the amount of this mass did not change after the second process, as expected (since the values of the expected densities, $\sigma_{expected}$, for this die are the same). For the protein die, again an additional mass is observed with $\sigma_{measured}$ being $1.14 \times 10^{-1} pg/\mu m^2$, resulting in a consistent ratio of hKOR/BSA masses (*=1.28*), which is very close to *85kDa/69kDa (=1.23)*. After the second process there is a mass increase corresponding to hKOR-antibody detection, which is consistent considering the one-sixth/seventh binding ratio with respect to the initial mass increase. Additionally, there is a one order of magnitude difference with the expected values and the measured ones. However, taking into consideration that the ratios of the measured masses (or surface mass densities) of BSA/hKOR and ratios of those in first/second processes are consistent with what is expected, the biological interaction of interest is specifically detected. Therefore, it is necessary to investigate the interaction mechanism or the effects of the bio-

chemicals, which are used in the functionalization processes, on the interaction scheme. In addition, a secondary imaging system is simultaneously necessary in order to see the actual state and structure of the adsorbate layer when utilizing an unprecedented molecule in sensing applications for the first time.

Chapter 6

CONCLUSION & OUTLOOK

6.1 Conclusion

In the course of this study, a theoretical model has been developed (and verified both theoretically and experimentally), clearly indicating the competing effects of stiffness and mass change on the shift in resonant frequency due to adsorption of a material. Using this more generalized approach, one can directly relate the resonance frequency shifts to the accumulated mass (for any stiffness mismatch between the sensor device and the adsorbate material), which is very important for many bio-chemical sensor applications that have to deal with analytes accumulated along the surface of the sensor micro-cantilever beam, such as the case of this study.

Additionally, some improvements have been carried out in the measurement setup in order to observe the potential powerful aspects of the diffraction grating interferometric readout technique more clearly. The mechanical noise immunity of this readout system is compared with a commercially available LDV system, demonstrating a more robust response to the same noise source. In addition, operation with higher order modes is carried out in both air and liquid in order to demonstrate suitability for measurements in aqueous

solutions with higher sensitivities. Therefore, this highly sensitive readout system, which also shows high immunity to environmental mechanical noise, proves to be a promising candidate for a low-cost and portable bio-selective mass sensor.

Furthermore, human κ-Opioid membrane protein is successfully immobilized on a cantilever surface for the first time and a specific detection of interaction between hKOR and drug-simulant His-antibody has been demonstrated. It may be possible to use such approach to detect narcotics from the biological samples.

6.2 Outlook

This study can be further extended in various ways, such as:

i. A more general and elaborate theoretical model, considering a mass accretion on a specific portion of the cantilever's active surface, can be developed in order to further isolate the effect of the position of where the accretion occurs from the effects of stiffness and mass changes.

ii. Simultaneous measurement of more than one cantilever, i.e. parallel reading-out of an array of cantilevers, can be realized for a high throughput bio-selective detection only with a low-cost self-oscillating feedback circuitry and a beam splitter introduced to the same measurement setup.

iii. The cantilevers can be actuated in aqueous solution for faster and more accurate results, and in vacuum to observe the sensitivity limits of the cantilevers and the measurement setup.

iv. The quality factor can be enhanced both in aqua and in air, changing the cantilever design parameters or simply with the aid of the very same self-oscillating electronic feedback circuitry mentioned above.

v. The quality factor, still, can be enhanced not only by limiting the measurement of resonance frequencies with the first order mode of the cantilever, rather observing higher order modes.

vi. Apart from increasing the quality factor, a real-time biochemical mass sensor device can be developed for monitoring the biochemical reactions dynamically in real-time, again with an electronic circuitry, especially a phase-locked loop (PLL) circuitry (for easier track).

vii. The detection of narcotics from biological samples can be done. Broad range of drugs can be detected by immobilization of other type of receptors.

With these sorts of improvements, this readout system will be a part of a low-cost and portable bio-selective mass sensor, which can be used in micro-gravimetric analyses.

Appendix A

MODAL ANALYSIS OF A UNIFORM BILAYER BERNOULLI BEAM WITH AN END LOAD

A.1 Uniform Bilayer Rectangular Bernoulli Beam [14]

The micro-cantilevers that are fabricated and used in the course of this study have rectangular cross section, as shown in Fig.2.1, consisting in the z-direction of two layers with different thicknesses (h_0 & h_1), elastic moduli (E_0 & E_1) and densities (ρ_0 & ρ_1). Different layers of the micro-cantilever are assumed uniform along its width (w) and length (L). The cantilever is in fixed-free configuration, i.e. fixed at one end $(y = 0)$, and free to move in the z-direction up to the other end. Bending due to the deflection of the cantilever, will cause an internal moment, M, given by [21],

$$M = w\int_h \sigma_{zz}\left(z - z_0\right)dz = -\kappa w\int_h E\left(z - z_0\right)^2 dz \qquad \text{(A.1)}$$

at any point along the cantilever length, where $\sigma_{zz} = -\kappa E\left(z - z_0\right)$ is the tensile stress due to the curvature (κ), E is elastic modulus, z_0 is the position of the neutral axis, and integral is over the total thickness (h) of the cantilever. For a uniform multilayer cantilever, E is a discontinuous, piecewise constant function of z. Since, the net longitudinal force,

straining the cantilever is zero; the net tensile stress over the cross section of the cantilever must also be zero. Therefore, the neutral axis can easily be determined as the solution to the equation (Eq.A.2.a),

$$w\int_h \sigma_{zz} dz = 0 \quad \Leftrightarrow \quad \int_h E\left(z - z_0\right) dz = 0 \tag{A.2.a}$$

as,

$$z_0 = \frac{1}{2}\frac{E_0 h_0^2 + 2E_1 h_0 h_1 + E_1 h_1^2}{h_0 E_0 + h_1 E_1} \tag{A.2.b}.$$

The flexural modes of the cantilever are governed by the equation of motion, which can be derived from Newton's second law as,

$$w\sum_{i=1}^{2}\left(h_i \rho_i\right)\frac{\partial^2 \zeta}{\partial t^2} = \frac{\partial^2 M}{\partial y^2} = -w\frac{\partial^4 \zeta\left(y\right)}{\partial y^4}\int_h E\left(z - z_0\right)^2 dz \tag{A.3}$$

where $\zeta(y)$ is the z-deflection at any point along the cantilever length. The small deflection approximation of the curvature is utilized in the derivation of equation (Eq.A.3) [21].

$$\kappa \approx \frac{\partial^2 \zeta\left(y\right)}{\partial y^2} \tag{A.4}$$

Assuming harmonic, modal solutions of the form,

$$\zeta_n(y,t) = \zeta_n(y)\cos(\omega_n t + \theta) \tag{A.5}$$

where ω_n is the angular resonance frequency of the n^{th} mode with an arbitrary phase θ, the equation of motion (Eq.A.3) simplifies to (Eq.A.6)

$$\frac{\partial^4 \zeta_n(y)}{\partial y^4} = \lambda_n^4 \zeta_n(y) \tag{A.6}$$

where the modal parameter λ_n is defined as,

$$\lambda_n^4 = \frac{\omega_n^2 (h_0\rho_0 + h_1\rho_1)}{\int_h E(z - z_0)^2 dz} \tag{A.7}.$$

The boundary conditions for a fixed-free cantilever are,

$$\zeta(0) = 0, \quad \zeta'(0) = 0, \quad \zeta''(L) = 0, \quad \zeta'''(L) = 0 \tag{A.8},$$

which state that the deflection and slope at the fixed end $(y = 0)$ is zero, and that the moment or shear force acting at the free end $(y = L)$ is also zero. After these boundary conditions are applied, the solutions to the simplified equation of motion (Eq.A.6) take the form of the flexural eigenmodes as,

$$\zeta_n(y) = A\left(\cos(\lambda_n y) - \cosh(\lambda_n y)\right) + B\left(\sin(\lambda_n y) - \sinh(\lambda_n y)\right) \tag{A.9}$$

with the modal boundary conditions

$$\frac{A}{B}=\frac{\cos\left(\lambda_n L\right)+\cosh\left(\lambda_n L\right)}{\sin\left(\lambda_n L\right)-\sinh\left(\lambda_n L\right)}=-\frac{\sin\left(\lambda_n L\right)+\sinh\left(\lambda_n L\right)}{\cos\left(\lambda_n L\right)+\cosh\left(\lambda_n L\right)} \tag{A.10}$$

which yield,

$$\cos\left(\lambda_n L\right)\cosh\left(\lambda_n L\right)+1=0 \tag{A.11}$$

The first five solutions of this equation are obtained numerically as

$$\lambda_n L=\left\{1.8751,\ 4.6941,\ 7.8548,\ 10.9955,\ 14.1372;\ \text{n=1,2,3,4,5}\right\} \tag{A.12}$$

and for higher order modes accurately approximate to $\lambda_n L\simeq\pi\left(n-\frac{1}{2}\right)$. The resonance frequencies f_n can then be obtained from (Eq.A.7) as,

$$\begin{aligned} f_n=\frac{\omega_n}{2\pi}&=\frac{\left(\lambda_n L\right)^2}{2\pi L^2}\sqrt{\frac{\int_h E\left(z-z_0\right)^2 dz}{\left(h_0\rho_0+h_1\rho_1\right)}} \\ &=\frac{\left(\lambda_n L\right)^2}{2\pi L^2}\sqrt{\frac{E_0^2h_0^4+4E_0E_1h_0^3h_1+6E_0E_1h_0^2h_1^2+4E_0E_1h_0h_1^3+E_1^2h_1^4}{12\left(E_0h_0+E_1h_1\right)\left(h_0\rho_0+h_1\rho_1\right)}} \end{aligned} \tag{A.13}$$

For a homogeneous, monolayer, rectangular cantilever beam, this expression becomes,

$$f_n = \frac{\lambda_n^2}{4\pi}\frac{h_0}{L^2}\sqrt{\frac{E_0}{3\rho_0}} \tag{A.14}.$$

A.2 Uniform Bilayer Rectangular Bernoulli Beam with an End Load

In order to apply the model to the micro-cantilevers with the platform containing the diffraction grating structures, the platform can be assumed an end load and the micro-cantilevers can be considered as uniform bilayer Bernoulli beams with an end load. Young [22] provides the resonance frequency of first order mode of a Bernoulli beam with an end load, which can be adapted for a monolayer micro-cantilever with a platform as an end load as,

$$f_n = \frac{1.732}{4\pi}\frac{h_0}{L^2}\sqrt{\frac{E_0}{3\rho_0\left(\frac{A_p}{wL}+0.236\right)}} \tag{A.15}.$$

From (Eq.A.15) the resonance frequency expression for first order mode of the micro-cantilever obtained in A.1 can be updated as,

$$f_n = \frac{1.732}{2\pi L^2}\sqrt{\frac{E_0^2h_0^4 + 4E_0E_1h_0^3h_1 + 6E_0E_1h_0^2h_1^2 + 4E_0E_1h_0h_1^3 + E_1^2h_1^4}{12\left(\frac{A_p}{wL}+0.236\right)\left(E_0h_0+E_1h_1\right)\left(h_0\rho_0+h_1\rho_1\right)}} \tag{A.16}.$$

BIBLIOGRAPHY

1. C. Ziegler, Cantilever-based Biosensors, Anal. Bioanal. Chem. 379 (2004), 946-959.

2. H. I. Ocakli, Fabrication and Characterization of Magnetic Microresonators, M.S. Thesis, Koc University, (August 2008)

3. A. Ozturk, Development of a Diffraction-Grating-Based Micro-Gravimetric Sensing Method for Biological Applications, M.S. Thesis, Koc University, (August 2008)

4. J. Tamayo, D. Ramos, J. Mertens, M. Calleja, Effect of the adsorbate stiffness on the resonance response of microcantilever sensors, Appl. Phys. Lett. 89 (2006), 224104

5. A. K. Gupta, et al, Anomalous resonance in a nanomechanical biosensor, Proc. Natl. Acad. Sci. U.S.A., 103-36 (2006) 13362-13367.

6. P. S. Waggoner, H. G. Craighead, The relationship between material properties, device design, and the sensitivity of resonant mechanical sensors, J. Appl. Phys. 105 (2009), 054306

7. M. Varshney, P. S. Waggoner, C. P. Tan, K. Aubin, R. A. Montagna, H. G. Craighead, Prion Protein Detection Using Nanomechanical Resonator Arrays and Secondary Mass Labeling, Anal. Chem. 80 (2008), 2141-2148

8. L. Johnson, A. K. Gupta, A. Ghafoor, D. Akin, R. Bashir, Characterization of vaccinia virus particles using microscale silicon cantilever resonators and atomic force microscopy, Sensor Actuat B-Chem, 115 (2006), 189-197.

9. N. V. Lavrik, M. J. Sepaniak, P. G. Datskos, Cantilever transducers as a platform for chemical and biological sensors, Rev. Sci. Inst., 75 (2004), 2229-2253.

10. M. L. Roukes, Nanoelectromechanical Systems: Potential, Progress, & Projections, IEEE MEMS 2007 (2007), 93-94.

11. K. L. Ekinci, Y. T. Yang and M. L. Roukes, Ultimate limits to inertial mass sensing based upon nanoelectromechanical systems, J. Appl. Phys., 95 (2004), 2682-2689.

12. D. Ramos, et al, Origin of the response of nanomechanical resonators to bacteria adsorption, J. Appl. Phys., 100 (2006) Art. No. 106105.

13. G. Y. Chen, T. Thundat, E. A. Wachter, and R. J. Warmack, "Adsorption-induced surface stress and its effects on resonance frequency of microcantilevers", J. Appl. Phys., 77 (1995), 3618-3622.

14. R Sandberg, et al, Temperature and pressure dependence of resonance in multi-layer microcantilevers, J. Micromech. Microeng., 15 (2005) 1454–1458

15. J.K. Luo, A.J. Flewitt, S.M. Spearing, N.A. Fleck, W.I. Milne, Young's modulus of electroplated Ni thin film for MEMS applications, Mat. Lett., 58 (2004), 2306-2309.

16. H. D. Espinosa, B. C. Prorok, Size effects on the mechanical behavior of gold thin films, J. Mater. Sci. 38 (2003) 4125 – 4128.

17. W. Nix, Met. Trans. A 20A (1989) 2217.

18. S. Okuda, M. Kobiyama and T. Inami, Mater. Trans.,JIM 40(5) (1999) 412.

19. A. Ozturk, H. I. Ocakli, N. Ozber, H. Kavakli, H. Urey, E. Alaca, A magnetically actuated resonant mass sensor with integrated optical readout, Phot. Tech. Lett., PTL-19423-2008

20. M. Baoa, H. Yang, Squeeze film air damping in MEMS, Sensor Actuat A-Phys, 136 (2007), 3-27

21. D. Sarid, Scanning Force Microscopy, Revised Edition, Oxford University Press, (1994), pp 1-18.

22. W. C. Young, R. G. Budynas, Roark's Formulas for Stress and Strain, 7th Edition, McGraw-Hill, (2001), p.766

VITA

Mehmet Salih Kılıç was born in Aydın, Turkey on 1981. He graduated from Izmir 60th Year Anatolian High School in 1999. He had his undergraduate studies in Bilkent University, Ankara, Turkey under full scholarship where he held his B.S. degree on physics. In 2007, he was accepted from Department of Mechanical Engineering in Koç University, Istanbul, Turkey for graduate studies. During his M. Sc. Studies he worked on biosensor applications of Micro-electromechanical Systems (MEMS) under supervision of Professor B. Erdem Alaca. His main interests of research include micro-nanofabrication, Scanning Probe Microscopy (SPM), MOEMS, NEMS, and eventually nanobiotechnology.

Following his M.Sc. thesis submission, he is going to pursue a Ph.D. degree under supervision of Professor B. Erdem Alaca in Department of Mechanical Engineering in Koç University, Istanbul, Turkey.